UNIVERSIDADE
BEIRA INTERIOR

Study of Electronic Speed Control Strategies for a Fixed Battery, Motor and Propeller Aircraft Propulsion Set

(versão final após defesa)

Viktor Zombori

Dissertação para obtenção do Grau de Mestre em
Engenharia Aeronáutica
(Ciclo de estudos integrado)

Orientador: Prof. Doutor Miguel Ângelo Rodrigues Silvestre

Covilhã, dezembro de 2021

Acknowledgements

I would like to express my gratitude to my supervisor, Professor Miguel Silvestre, for all the guidance provided throughout the realization of this thesis.

I would also like to thank Jorge Rebelo and Pedro Alves for sharing their time and knowledge, which were crucial to make the present work happen.

A special thank you to my family for their love and support in every way.

A big thank you to my friends for all the great moments and for always being there.

Resumo

No âmbito da participação da equipa AERO@UBI no Air Cargo Challenge 2021/2022, foi realizado um estudo de um sistema propulsivo elétrico com duas hélices como opção e uma bateria e motor definidos. Os objetivos passavam por maximizar a tração gerada pelo conjunto, especialmente a elevadas velocidades de vento relativo, através da adoção da melhor estratégia de controlo do motor e escolher a melhor das hélices para este propósito. Dois controladores eletrónicos de velocidade foram selecionados: o Phoenix ICE 75 da Castle Creations, que realiza comutação trapezoidal, e um A50S da Team Triforce, que opera com field-oriented control (FOC). Ambos foram testados em condições de tração estática e com vento relativo, utilizando uma bancada de tração estática e uma instalação experimental montada em um túnel de vento, respetivamente. Estes testes permitiram perceber qual a influência de diferentes funcionalidades implementadas nos controladores tais como motor timing e frequência de modelação de comprimento de pulso (PWM rate), bem como várias magnitudes de field weakening. Os resultados obtidos foram muito positivos: em condições estáticas, o FOC com field weakening permitiu aumentar a tração estática produzida em mais de 10% relativamente ao melhor valor obtido com a comutação trapezoidal. Esta diferença foi amplificada ainda mais com velocidades crescentes de vento relativo.

Palavras-chave

Motor elétrico, controlo de motor, field-oriented control, field weakening, hélice.

Abstract

A study of an electrical propulsion system with two propeller options and a fixed battery and motor was performed, in the context of the participation of the AERO@UBI team in the Air Cargo Challenge 2021/2022. The goals were to maximize the thrust generated by the setup, specially at high relative wind speed, by means of adopting the best motor control strategy and to select the better propeller for this purpose. Two electronic speed controllers (ESCs) were selected: the Castle Creations Phoenix ICE 75, that performs trapezoidal commutation, and a Team Triforce A50S, which makes use of field-oriented control (FOC). Both were tested under static condition and with relative wind, using a static thrust stand and an experimental setup in a wind tunnel, respectively. These tests allowed to understand the influence on the generated thrust and drawn current of different settings that are implemented on the controllers, such as motor timing and pulse-width modulation (PWM) rate, as well as various magnitudes of field weakening. The obtained results were very positive: under static conditions, FOC with field weakening allowed to increase the generated static thrust by more than 10% relative to the best value obtained with trapezoidal commutation. This difference was amplified even more with increasing relative wind speed.

Keywords

Electric motor, motor control, field-oriented control, field weakening, propeller.

Contents

List of Figures

List of Tables

List of Abbreviations

ACC	Air Cargo Challenge
BEC	Battery Elimination Circuit
BEMF	Back Electromotive Force
BLDC	Brushless Direct Current
CL	Castle Link
d	Direct axis
DC	Direct Current
EMF	Electromotive Force
FOC	Field Oriented Control
FW	Field Weakening
IGB	Insulated-Gate Bipolar Transistor
MSc	Master of Science
MOSFET	Metal–Oxide–Semiconductor Field-effect Transistor
PI 75	Phoenix ICE 75
PID	Proportional-Integral-Derivative
PMSM	Permanent Magnet Synchronous Motor
PWM	Pulse-Width Modulation
q	Quadrature axis
RC	Radio Controlled
RPM	Revolutions per Minute
RMS	Root mean square
UBI	University of Beira Interior
VCC	Positive Supply Voltage

List of Symbols

C_T	Thrust coefficient
C_P	Power coefficient
H	Distance between the ball bearing axis and the motor axis, m
i	Motor current, A
I_a	Phase A current, A
I_b	Phase B current, A
I_c	Phase C current, A
J	Advance ratio
K_Q	Motor torque constant, N.m/A
K_V	Motor speed constant, rad/s/V
L	Distance between the ball bearing axis and the touching point on the scale, m
$L_d - L_q$	Motor Inductance Difference, H
n	Motor speed
N_{poles}	Number of magnetic poles in a motor
P	Power, W
P_{atm}	Atmospheric pressure, Pa
P_s	Static pressure, Pa
P_{shaft}	Shaft power, W
Q	Torque, N.m
Q_m	Shaft torque, N.m
R	Motor resistance, Ω
T	Thrust, N
T_{atm}	Air temperature, ºC
v	Motor terminal voltage, V
V	Freestream velocity, m/s
v_m	Internal BEMF of the motor, V
η_m	Motor efficiency, %
θ_{mech}	Mechanical rotation angle, degree
θ_{elec}	Electrical rotation angle, degree
λ	Motor Flux Linkage, Wb
ρ	Air density, kg/m^3,
Ω	Mechanical angular velocity, rad/s

Chapter 1

Introduction

1.1 Motivation

The Air Cargo Challenge (ACC) is an international competition that attracts aeronautical and aerospace engineering students from all over the world. It is held every two years in Europe and made its debut in 2003 thanks to the Portuguese Association of Aeronautics and Space (APAE). It offers students the opportunity to create an aircraft from scratch, and it is guided by a set of rules and objectives.

The competition is based on a point system. In the 2021/2022 ACC edition [1] several items will be taken into consideration: design report, video presentation, technical drawings and flight competition. Within the flight competition, aspects such as transported payload, traveled distance, achieved altitude, loading and unloading time, payload prediction and take-off distance will be evaluated. Most of these performance parameters are directly affected by the performance of the propulsion system.

Figure 1.1: Some of UBI participations in the ACC in previous years.

When it comes to the propulsion system, past editions (see figure 1.1) of the competition had a few different limitations that aimed to make the challenge as fair as possible. In the 1^{st}

edition with electrical motorization (held in Portugal, in 2007), only the motor model and the maximum allowed current were defined. In the 2^{nd}, a device was measuring the current throughout the flight and if it exceed a certain value, the team would lose points. In the 3^{rd}, an electronic device was installed on the aircraft in order to limit the throttle input. The 4^{th} edition was the first time that the propeller was pre-selected. For the 2021/2022 edition, the goal is to build an electrical unmanned aircraft with the virtual task of transporting medical goods. The motor is defined by the rules and the battery is limited to a 3S li-po. A choice between two propellers is allowed. There is freedom to choose the electronic speed controller (ESC) as long as it is commercially available, so one way of improving the performance of the propulsion system is by optimizing the motor control, which will be the focus of the present work.

1.2 Scope

This particular study aims to maximize the performance of the propulsion system by means of ESC selection and its settings. The output power and generated thrust will be measured in static condition and with relative wind for trapezoidal commutation and field-oriented control (FOC). Field weakening implementation will also be studied as a mean of increasing the thrust at high relative wind speed, given the 3S battery voltage limitation. The overall goal is to find out what control strategy should be used to maximize the thrust available to the ACC aircraft. Although it is directly targeted for this competition, the collected results should be helpful for any systems that use brushless motors such as cars, skateboards, multi-copters, etc. Since one of two different propellers may be used, they will also constitute one of the variables of this study.

1.3 Objectives

- Understand how every parameter changed in the ESC affects the thrust produced and current consumed by the set;
- Obtain static thrust and motor current consumption values for the different control strategies and propellers;
- Characterize the thrust produced and current consumed as functions of relative wind speed for the different control strategies and propellers;
- Find out what control strategy and propeller should be used in the ACC aircraft in order to maximize its performance.

1.4 Document Structure

This dissertation has the following structure:

- Chapter 2 presents a brief literature review starting by a summary of important concepts regarding electric motors and their control as well as description of the state of the art of motors and speed controllers;

- Chapter 3 documents the methodology that was followed in order to prepare the ESCs, motor and propellers for the static and dynamic tests, as well as the procedures of the tests themselves;

- Chapter 4 presents the results of the tests of the different propellers, ESCs and settings, as well as a discussion of these results;

- Chapter 5 summarizes the conclusions and provides some recommendations for future work.

Chapter 2

Literature Review

2.1 Fundamentals

2.1.1 Brushed DC Motor

As the name suggests, brushed motors make use of brushes. These are internal electrical commutators that reverse the polarity of the active wire coils as they go through the magnets.

There are 3 main parts in a brushed motor: the stator, the rotor, and the commutator [2]. A scheme of the general design is shown in figure 2.1.

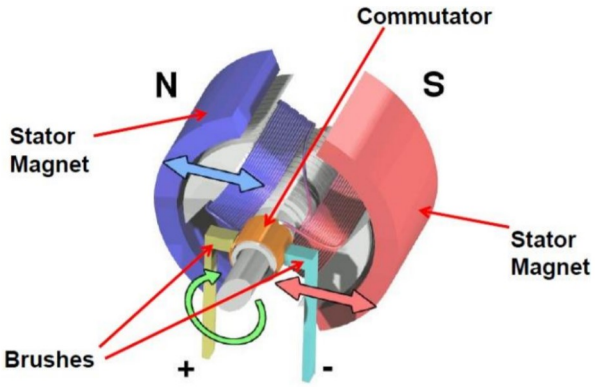

Figure 2.1: Brushed DC Motor design [3].

The stator contains the permanent magnets. Instead, an electromagnet could be used in a shunt, series or compound configuration, but they make it harder to maintain a magnetic field in smaller motors. The permanent magnets are arranged in pairs of alternating north-south, so there is always an even number of magnets in a motor.

The rotor contains the armature, which consists of windings of copper wire. When receiving energy, half of the armature will have an electrically induced magnetic north pole that will be attracted to the south poled permanent magnet, while the electrically induced magnetic south pole armature will be attracted to the north poled permanent magnet. This will cause the stator and rotor to rotate towards a state of equilibrium. As the motor approaches this state, the commutator inverses the magnetic polarity of the armature, which forces it to keep rotating towards the now new state of equilibrium. More coils of wire connected to more segments of the commutator can be used in order to reduce the speed and torque fluctuation and make the motor run more smoothly and efficiently.

There are a few advantages and disadvantages of this type of motor [4]. They are cheaper and easier to make in smaller sizes. There is also no need for an ESC, since the speed is controlled via the bus DC voltage. The main disadvantage is the wear-out of the brushes. Another one is that these motors create a lot of electromagnetic interference due to brush arcing, which causes heat. At last, the inefficiency of this type of motor grows with speed, in part due to the contact friction of the brushes.

2.1.2 Brushless DC Motor

A brushless motor is, as the name suggests, a motor without brushes. It is composed of a stationary part, called the stator, which contains the copper windings and a rotating part, called the rotor, which contains the permanent magnets [2]. As this type of electrical motor does not make use of brushes or any other mechanical commutators in order to run, the commutation has to be performed externally on a device called Electronic Speed Controller.

The most common configurations are axial-flux and radial-flux, with the radial-flux being much more popular. In this category, there are inner-rotors and outer-rotors. In the inner-rotors, the rotor is located in the inner side, while in the outer-rotors, the rotor is located in the outer side of the motor. The differences can be seen in Figure 2.2. Inner-rotors usually have a lower diameter, lower rotor inertia and high power due to high rotational velocity with a limited torque. They are used in robotics, manufacturing and tools such as pumps, conveyors, compressors. Outer-rotors usually have a larger diameter and a larger rotor inertia and torque production, which makes it better for constant speed applications such as fans, direct drive machine tools and vehicle propulsion.

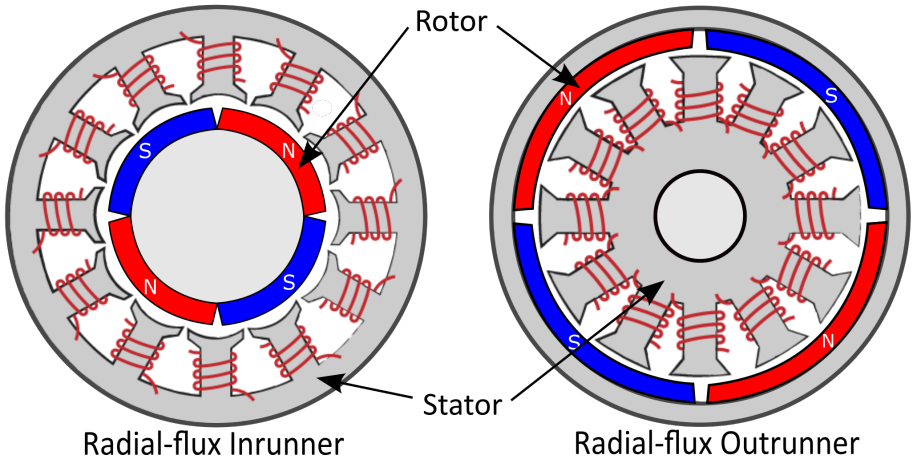

Figure 2.2: Radial-flux inrunner and outrunner diagram (adapted from [5]).

An individual group of windings that lead to a single terminal outside of the motor is called a phase. The majority of brushless motors are 3-phased. A pole is a single permanent magnet pole, north or south. In the figure above, each of the motors has 2 pairs of poles. At least a pair of poles must exist and there is no theoretical limit for the number of pairs.

The lack of brushes means that there is less friction, which allows brushless motors to operate at higher speeds, have less heat production and overall higher efficiency. They also have higher output power to size ration and last longer than the brushed motors. Although the need for an external ESC makes this motor more costly and complex, the fast development of technology almost eliminates this factor.

In electric motors, there is a difference between mechanical and electrical rotations or angles. The mechanical angle is the physical angle that the rotor rotates relative to the stator, so a 360 degree rotation would mean that the rotor completed one revolution, which can be observed directly. The electrical angle corresponds to the angular rotation of the flux and depends on the number of poles the motor has. If a given motor has 1 pair of poles,N_{poles}, the electrical rotation would equal the mechanical rotation, but if a motor has 2 pairs of poles, making a rotation of 360 mechanical degrees, θ_{mech}, would mean that it completed 720 electrical degrees, θ_{elec}, according to equation 2.1.

$$\theta_{elec} = \theta_{mech}.N_{poles} \tag{2.1}$$

2.1.2.1 Theoretical Model

There are many models of electrical motors, ranging from simplistic to very complex ones. Here, the first-order model of the DC electric motor [6] will be discussed, which quickly helps to predict the behavior of a DC motor. Figure 2.3 shows the circuit that is equivalent to a DC motor.

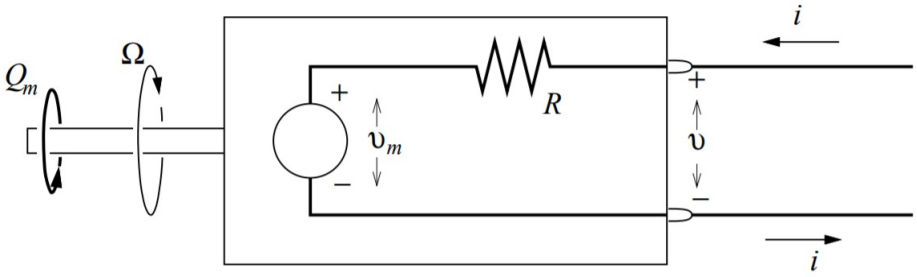

Figure 2.3: Equivalent circuit for a DC electric motor [6].

R is the resistance at the terminals of the motor and is assumed constant.

Q_m is the shaft torque and is assumed to be proportional to the current i via K_Q, the torque constant, minus a friction torque loss related current i_o.

$$Q_m(i) = (i - i_o)/K_Q \tag{2.2}$$

v_m is the internal back electromotive force (BEMF) and is assumed to be proportional to the

mechanical angle velocity Ω via K_V, the motor speed constant.

$$v_m(\Omega) = \Omega / K_V \tag{2.3}$$

The motor terminal voltage is then obtained by adding on the resistive voltage drop.

$$v(i, \Omega) = v_m(\Omega) + iR = \Omega / K_V + iR \tag{2.4}$$

We can now manipulate this equations to obtain current, torque, power and efficiency values, as functions of the motor speed and voltage at its terminals.

$$i(\Omega, v) = (v - \frac{\Omega}{K_V})\frac{1}{R} \tag{2.5}$$

$$Q_m(\Omega, v) = [i(\Omega, v) - i_o]\frac{1}{K_Q} = [(v - \frac{\Omega}{K_V})\frac{1}{R} - i_o]\frac{1}{K_Q} \tag{2.6}$$

$$P_{shaft} = Q_m \Omega \tag{2.7}$$

$$\eta_m(\Omega, v) = \frac{P_{Shaft}}{iv} = (1 - \frac{i_o}{i})\frac{K_V}{K_Q}\frac{1}{1 + iRK_V/\Omega} \tag{2.8}$$

In the case of zero friction ($i_o = 0$) and zero resistive losses ($R = 0$), the equation of efficiency (2.8) becomes

$$\eta_m = \frac{K_V}{K_Q} \tag{2.9}$$

So, for energy to be conserved, the torque constant K_Q must be equal to the speed constant K_V. In these equations K_V is in rad/s/V and K_Q is in the equivalent unit of A/Nm. However, K_V is usually presented in revolutions-per-minute/V (RPM/V).

The motor speed constant is an important value for brushless motors and it is always provided by the motor manufacturers. It corresponds to the number of RPM that a motor makes, for each Volt that is applied to it, with no load attached. By knowing this value, it is possible to quickly find out how fast the motor rotates for a given battery or power supply.

2.1.2.2 Motor Parameter Measurement

- Motor Resistance

  The motor resistance R can be obtained by using a multimeter (or ohmmeter) to measure the resistance, although usually the values are too that so an accurate value is hard to obtain. Alternatively, a current i can be fed across two terminals of the motor, while measuring the voltage v across it. Then, resistance R can be calculated from Ohm's Law (2.10).

$$R = v/i \tag{2.10}$$

- Zero-load Current

  Zero-load current, i_o can be measured by applying a voltage v to the motor, and then running it at full throttle, with nothing connected to its shaft. For the typical brushless outrunner motor used in the Air Cargo Challenge UAV size class, a 10 V power supply is usually used. Although the simple motor model considers constant friction torque, in reality, a higher angular velocity normally results in a higher friction torque. Therefore, the specification of i_o of the motor is typically followed by the voltage used for that test.

- Speed Constant

  The speed constant can be computed from (2.3):

$$K_V = \frac{\Omega}{v_m} \tag{2.11}$$

  where v_m, the back-EMF voltage, can be calculated with the previously obtained resistance R, voltage v and zero-load current i_o.

$$v_m = v - i_o R \tag{2.12}$$

- Torque Constant

  The Torque Constant K_Q can be obtained from motor torque data. According to torque model (2.2), Q_m plotted against $i - i_o$ is a straight line crossing the origin. The slope of this line then gives $\frac{1}{K_Q}$. As can be observed from (2.9), any difference between K_Q and K_V will result in an efficiency lower than 1, and may be an indicative of the imperfections of this motor model. Alternatively, K_Q may simply be assumed equal to K_V.

2.1.3 Brushless Speed Control

As brushless motors do not have a commutator, a dedicated external speed controller is needed. These electronic speed controllers, usually take a DC power input and a Pulse-Width Modulation (PWM) duty cycle input signal and output a voltage and current for each phase of the motor as functions of the motor electrical angle position, in order to keep it a certain operating condition [7]. The phase current should ideally replicate the motor's BEMF, which is discussed in subsection 2.1.4. The more basic controllers apply voltage over two of the three phases of the motor, which creates an electromagnetic field around them. As the permanent magnets are attracted or repelled by this electromagnetic field, they cause the rotor to move. The controller then switches the phases and the magnets are attracted to another electromagnetic field. As long as this electronic phase shifting keeps happening, the rotor will keep chasing the electromagnetic field created by the stator and the motor will keep running. More advanced controllers can power the 3 phases simultaneously. This allows for a more efficient and smoother operation of the motor, at the expense of higher ESC complexity and computational cost.

There are 3 main parts to an ESC: the position sensing, the processor, and the gates (also called inverters). The first one is responsible for reading the motor's electrical position, which can be achieved with or without position sensors. The processor takes the input from the first one as well as input from the user to calculate when and which gates should be switched. The gates are responsible for connecting or disconnecting a given motor terminal to or from the DC supply. For this, electronic power switches are used. They are usually MOSFETs (Metal–Oxide–Semiconductor Field-effect Transistors) or IGBTs (Insulated-Gate Bipolar Transistors). The MOSFETs resistance is constant, so the voltage drop across its terminals increases with current, while the IGBTs voltage drop remains constant because the resistance changes with current. Thus, the first ones are usually used with lower power applications because that is when they have less resistance, while the latter ones are used in systems with higher voltages [8].

2.1.4 BEMF

As the motor rotates, it induces a counter-electromotive force on the motor phases due to magnetic induction [8], following Faraday's law. For instance, when a motor is disconnected from a power source and connected to an oscilloscope, rotating the motor manually will produce a BEMF that can be measured. This voltage is a function of the electrical position angle of the rotor and its magnitude is proportional to the angular velocity of the motor, so by measuring it, the angular velocity of the motor can be determined.

Depending on the shape of their BEMF, brushless motors can be differentiated into two types: BLDC and PMSM. BLDC motors characteristically have a more trapezoidal BEMF, while PMSM motors have a more sinusoidal BEMF. Figure 2.4 shows the ideal trapezoidal and sinusoidal BEMF waves, normalized to root mean square (RMS) of 1.

Magnet and stator core geometry, magnetization and winding distribution are some properties of the motor design that affect the shape of the BEMF [9].

The working principle of both BLDC and PMSM is the same. The difference is that in a PMSM, the coils of the stator are wound in a sinusoidal manner.

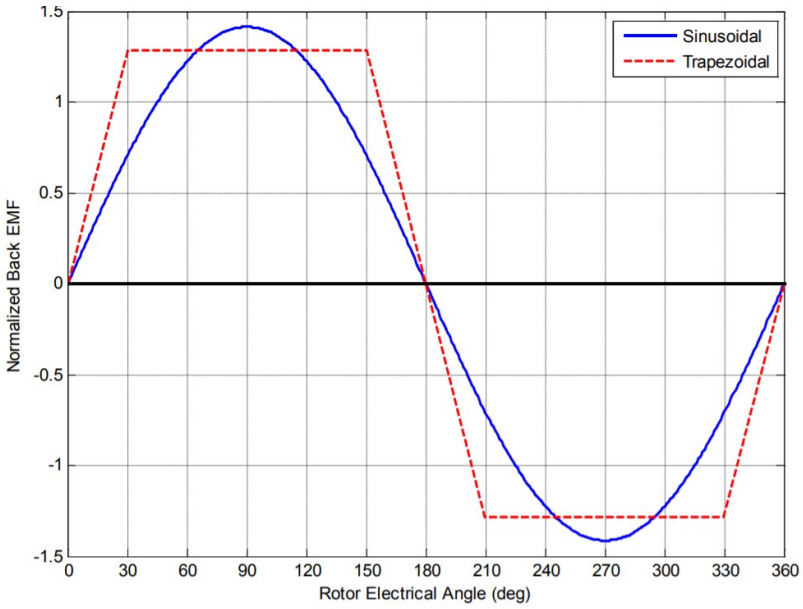

Figure 2.4: Ideal sinusoidal vs. trapezoidal back EMF waveforms, normalized to RMS=1 [9].

2.1.5 Sensored and Sensorless Control

2.1.5.1 Sensored

The simplest way of knowing the electrical position of the motor rotor is by using a position sensor. This type of sensor sends information about the position of the motor rotor to the controller, which then uses it to drive the motor in the most effective way. The most common devices for this are Hall effect sensors and magnetic or optical encoders [10].

When using sensors, the motor is able to rotate more smoothly and with more torque right from zero RPM, thus this type of motor is used when low constant speeds or high position precision is needed, for example, in drills or camera gimbals.

2.1.5.2 Sensorless

Sensorless motor control can be performed through flux measurement or BEMF wave detection methods [11]. The first one is more complicated and more costly in terms of hardware and processing, thus BEMF detection methods are usually preferred commercially and industrially [12]. Since the motor does not generate any BEMF at zero RPM, it has to be rotating at a minimum speed in order to generate BEMF that allows to apply these methods. So, at zero RPM, the ESC drives the motor in open-loop [13], which means that it tries to rotate the motor without feedback. This sometimes results in jerking of the motor which is not seen

in sensored control. Once the motor is running at a sufficient speed, the generated BEMF allows the algorithm in the controller to estimate the rotor position and drive the motor in a closed-loop. Although sensorless control is not very good at low speeds, it performs really well at high speeds, which is one of its advantages over the sensored control. It is also lighter but requires more computational power. This type of control is used a lot in radio-controlled (RC) model aircraft and Air Cargo Challenge sized UAVs, because they tend to operate at higher speeds and the starting torque needed to rotate the propeller is very low.

2.1.6 Motor Control - Trapezoidal, Sinusoidal and FOC

2.1.6.1 Trapezoidal

With this method, one of the three motor terminals is off at any time, the other is sinking current, and the last one is sourcing current. For this, and in the same order, one of the phases is un-energized, the other is connected to the positive DC power supply terminal, and the last one is connected to the negative DC power supply terminal [14]. This generates a magnetic field in the stator, which interacts with the magnets and makes the rotor spin. Recurring to position sensors or BEMF sensing, the controller switches the phases in order to keep it spinning. Figure 2.5 illustrates the behavior of trapezoidal motor control. The hall sensor output can be seen, as well as the BEMF, the torque the motor outputs and the phase current shifting.

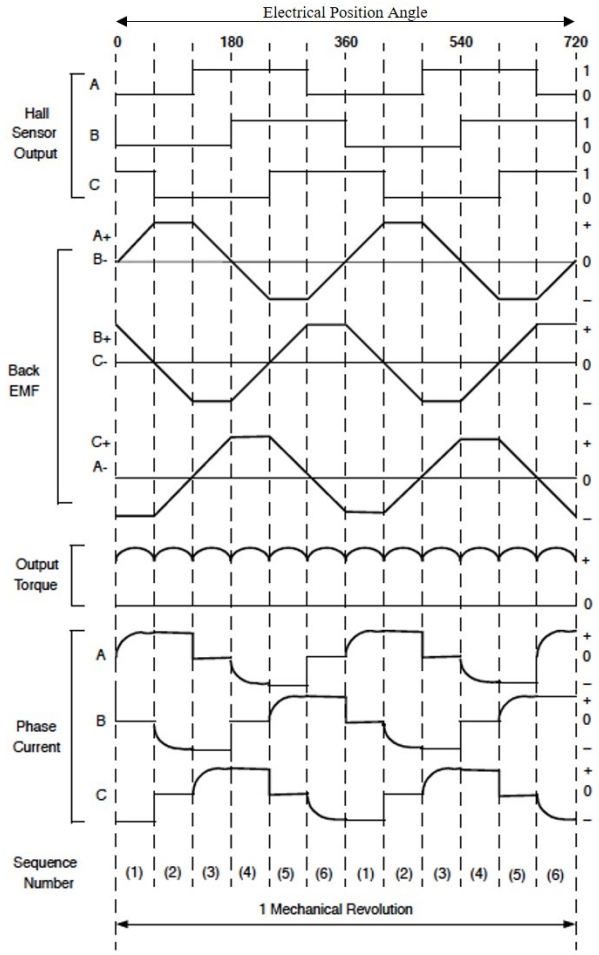

Figure 2.5: Hall sensor signal, BEMF, output torque and phase current waveforms of an electrical motor with trapezoidal BEMF as function of electrical position angle (adapted from [15]).

The resulting waveform is almost of trapezoidal shape, depending on the motor inductance. Simplicity and cost effectiveness are the main advantages of this type of control, but it also has some disadvantages, such as torque ripple.

2.1.6.2 Sinusoidal

Sinusoidal commutation is used in motors with a sinusoidal back EMF, which are considered AC motors. In this type of commutation, current is injected simultaneously in all the phases of the motor (see table 2.1) in the form of sine waves. In reality, these waves are generated with high frequency PWM square waves, which then, with the inductance of the motor, are filtered into sinusoidals. For this type of commutation, a high resolution position sensor such as an encoder is recommended, which is why this is a more expensive solution. Although it reduces the torque ripple and noise that is present in the trapezoidal commutation, sinusoidal commutation is not as good as trapezoidal beyond a certain electrical speed. In the case of the ACC motor-propeller setup, the electrical speed is high enough to allow sensorless sinusoidal control, but possibly low enough to still have an efficient control compared to the trapezoidal ESC.

Motor Position				Inverter State			
Interval (degrees)	Hall A	Hall B	Hall C	ON Switches	Phase A	Phase B	Phase C
0 to 60	1	0	1	S1, S6, S5	+	-	+
60 to 120	1	0	0	S1, S6, S2	+	-	-
120 to 180	1	1	0	S1, S3, S2	+	+	-
180 to 240	0	1	0	S4, S3, S2	-	+	-
240 to 300	0	1	1	S4, S3, S5	-	+	+
300 to 360	0	0	1	S4, S6, S5	-	-	+

Table 2.1: Switching sequence for sinusoidal commutation [8].

PWM is a way of controlling the current delivered to the phases of the motor by turning the circuit on and off in pulses of different duration. Consider a load where the power supply is on during half of the considered time frame and off during the other half. The mean current level would be half of the state where the power supply is on during the whole period. Thus, the current level is proportional to the on time-fraction.

Figure 2.6 exemplifies how a sinusoidal current can be generated using square PWM waves. In this circuit, a comparator is fed with a reference sinusoidal wave signal, U_{rsw}, in the positive terminal that is compared with a triangular wave signal in the negative terminal, U_{tw}. When $U_{rsw} > U_{tw}$, $S_A = 1$, which generates a pulse to the gates driver. During the duration of the pulse, the upper left gate and lower right gate close the circuit, applying +V_{DC} to the phase A of the motor. During this condition, I_A increases in time with an increase rate proportional to the motor inductance. When $U_{rsw} < U_{tw}$, -V_{DC} is applied to the phase A of the motor, making I_A decrease in time. This results in a sinusoidal current with a small amount of ripple, due to the motor inductance.

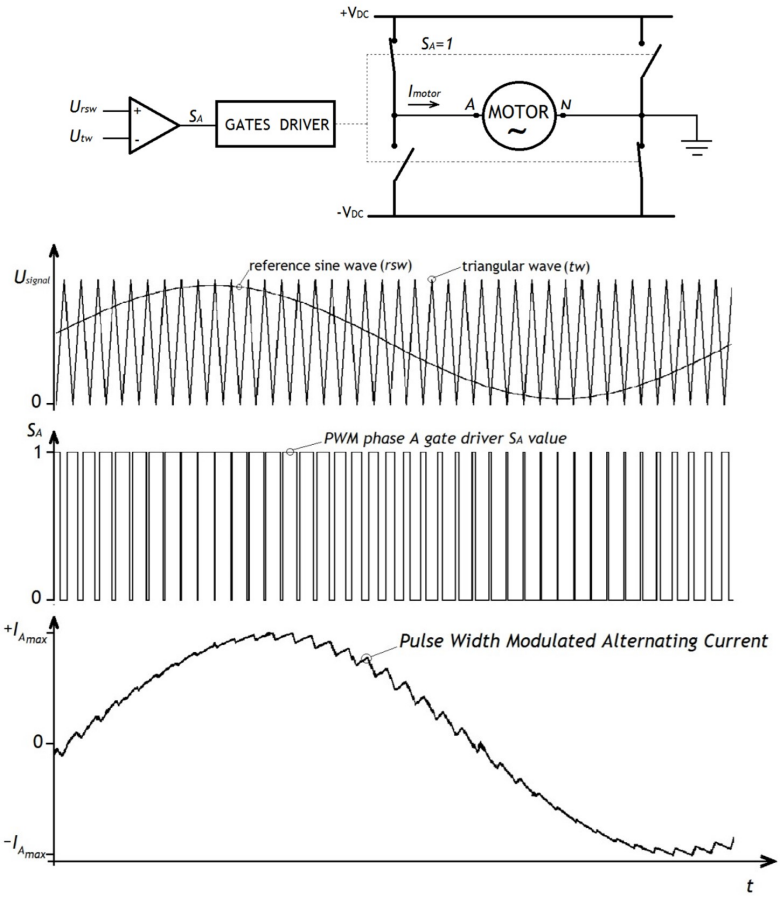

Figure 2.6: Sinusoidal wave generation with PWM [8].

2.1.6.3 Field-Oriented Control

Field-oriented control is a more advanced technique that transforms the 3 phase currents in 2 separately controlled components: torque and flux [16]. First, the 3 phase sinusoidal currents (I_a, I_b, I_c) are transformed into a two-phase (α, β) system that varies in time through the Clarke transformation. Then, α and β are transformed into the d,q reference frame using the Park's transformation. In this two-coordinate time invariant system, the direct-axis represents the flux, which depends on the rotor's electrical position, and the quadrature-axis represents the torque, which depends on the current, and is 90º apart from the d-axis [17]. At this point, and according to the torque necessary, d and q can be adjusted. The d-axis has a magnetising or demagnetising effect on the motor, so this component is usually required to be zero in order to maximize the motor's torque (q-axis) and efficiency.

After the d and q values are defined, they are transformed back into the stationary reference frame through the inverse Park's and Clarke's transformation, resulting in the time dependent 3-phase currents. The output of the inverse Clarke transformation provides the duty cycles of the PWM channels corresponding to the three phase voltages. Space Vector Modulation may then be used or not, depending on the chosen control algorithm [18]. These steps are illustrated in Figure 2.7.

This type of control is much more demanding on the hardware, thus requiring more complex and expensive components.

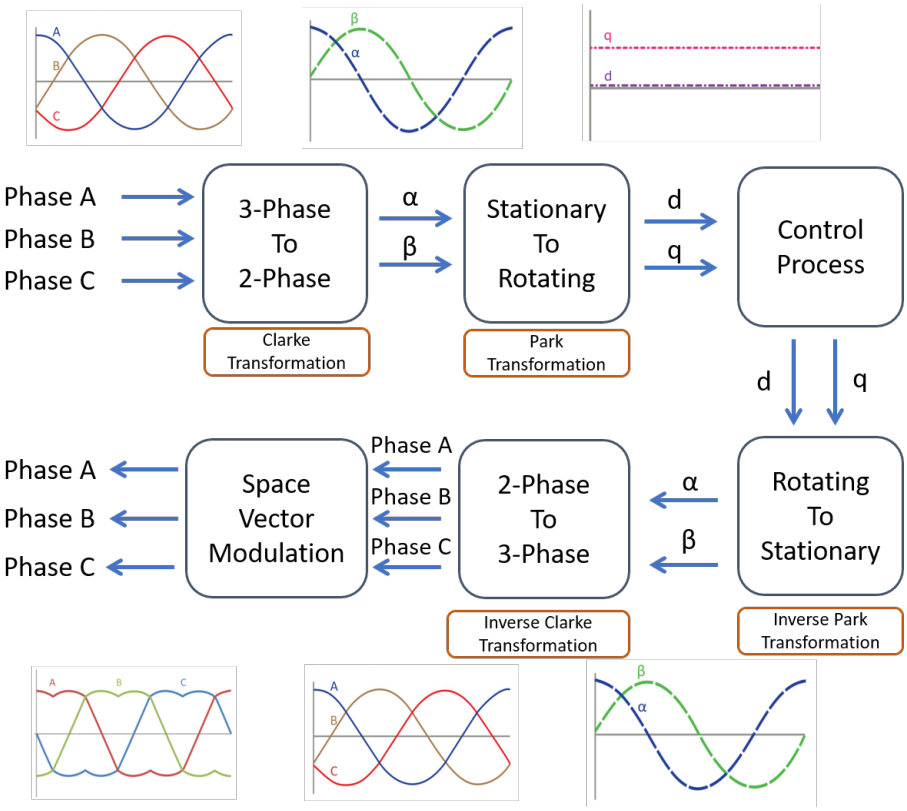

Figure 2.7: Field-oriented control structure.

Table 2.2 shows the main similarities and differences between the 3 commutation methods discussed above.

Technique	Trapezoidal	Sinusoidal	FOC
Start-Up Power	High starting torque, but lots of ripple	Lower but smoother starting torque	Lower starting Torque
Power Delivery	High torque ripple	Smooth	Smooth
Speed Control	Excellent	Excellent	Excellent
High Speed Performance	Good	Poor	Excellent
Controller Complexity	Low	Medium	High

Table 2.2: Commutation Methods Comparison (adapted from [19]).

2.1.7 Field Weakening

As established earlier, when a motor rotates, it creates a back EMF voltage that is proportional to the speed of rotation. In order to push current into the coils, the supplied voltage must be greater than this BEMF voltage. The limit is reached when the speed is such that the BEMF voltage is the same as the supplied voltage, and the inverter can no longer push current into the stator coils. This means that for a given voltage supply, there is a maximum rotational speed for a given motor: the base speed [20].

In order to exceed this speed, the BEMF voltage needs to be reduced, and this can be achieved by forcing negative current to the d axis of the motor, which causes the rotor magnets magnetic flux to be reduced, and lowers the BEMF. With this, it is possible to achieve higher rotational speeds. On the other hand, torque is proportional to field flux, so, while the rotational speed is increased, the torque is reduced, thus, requiring more current to reach the same motor torque. Therefore, the motor efficiency is reduced.

This region is shown in Figure 2.8, where the maximum torque, maximum power and maximum rotor flux are plotted. Only the shape of the plots should be considered. This effect can be seen as an increase of the K_V of the motor, in exchange for efficiency.

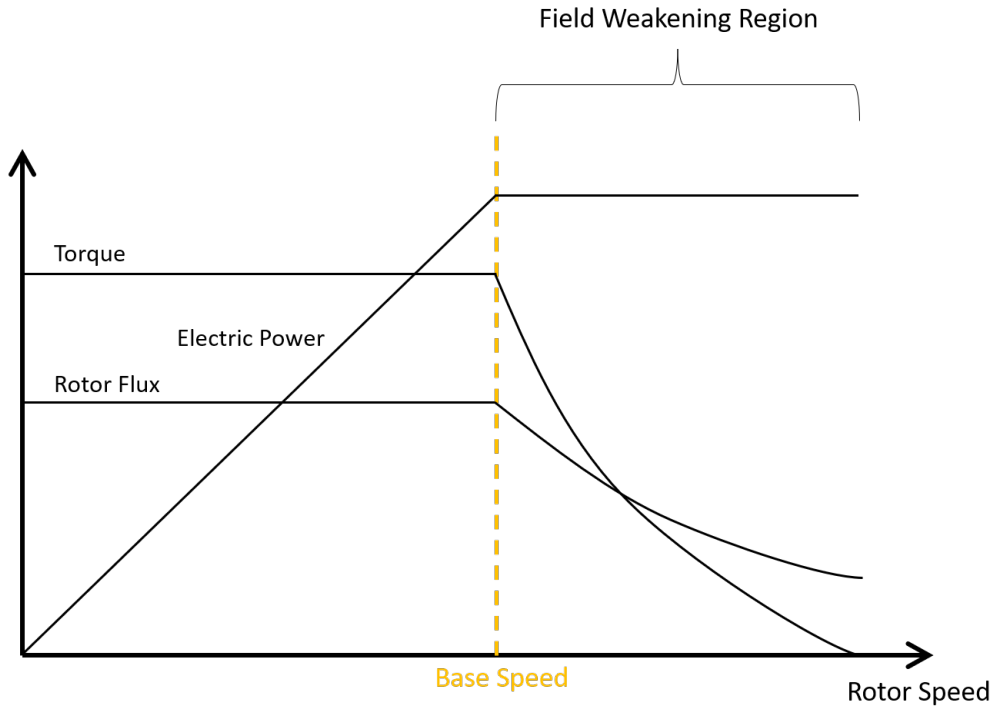

Figure 2.8: Field weakening region (adapted from [21]).

2.2 State of the Art

There are many recent studies that aimed to add something new and better to the motor control strategies discussed earlier. On the other hand, no studies were found regarding the influence of the control strategy on the performance of a motor-propeller system and how it would relate with the actual performance of the aircraft. Trapezoidal commutation is still very much in use, but it is becoming outdated, which is why the most recent studies tend to focus on FOC, which is becoming the standard as the technology evolves. The studies mentioned next are mainly related to FOC and field weakening, because these are areas that still need to be studied and continue to have room for improvement.

Alessandro Bosso et al [22], documented his work in developing a computationally-effective

field-oriented control strategy by integrating a recent sensorless observer into the system, without requiring any information of the mechanical dynamics and their parameters.

Micael Ratcliffe and Kelum Gamage [19] from Lancaster University proposed a new power control technique that aimed at reducing switching losses by centering the driving current around the optimum flux interaction point and bringing the PWM frequency down to that of the commutation frequency.

Hastanto Widodo et al [23], proposed a novel electronic speed controller with rotor field control in addition to standard motor power control. In order to approach the ideal BLDC motor concept, an automotive generator was converted into a BLDC motor. Unlike a normal BLDC motor, which has a standard power curve characterized with maximum power which is only achievable in one specific speed, the proposed setup could allow the motor to have an adjustable maximum power in a wide range of operation speeds.

The physical components present in the ESC also affect its performance. Part of the study made by Young Tae Shin and Ying-Khai Teh [24] focused on how the type of power transistor would affect the overall efficiency of a small commercial quadcopter UAV. They compared a few models of transistors with Si-IGBT (Silicon-based Insulated Gate Bipolar Transistor), SiC (Silicon Carbide Semiconductor) and GaN (Gallium Nitride Semiconductor) technology and translated that to the flight time that a specific drone would have if using each.

The effect of field weakening can also be improved by designing the motor for that purpose. Senol and Uston [25] developed a BLDC motor with higher direct-axis phase inductance, which provided a better performance in the field weakening region.

The literature survey allowed to conclude that the the present work is a novelty in the electric aircraft motor control field, given that there were not found any similar studies on control methods or field weakening effects on the performance of a propeller aircraft.

Chapter 3

Methodology

3.1 Motor

The motor used was defined by the Air Cargo Challenge rules: the AXI 2826/10. This is a PMSM outrunner type of motor, with 7 pairs of poles in the rotor. At the time of the realization of this study, there were 2 available options, the AXI 2826/10 GOLD LINE and the newer AXI 2826/10 GOLD LINE V2. A picture and a technical drawing of each is shown in Figure 3.1.

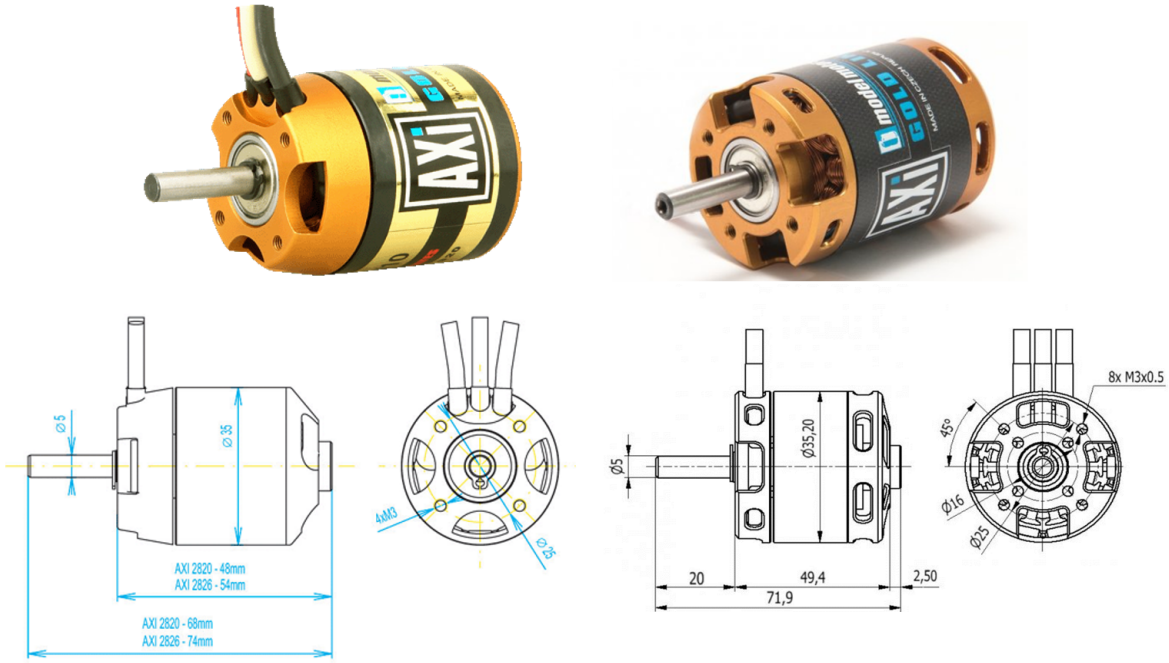

Figure 3.1: On the left: AXI 2826/10 GOLD LINE, on the right:AXI 2826/10 GOLD LINE V2 [26]

The specification of each motor are shown in Table 3.1.

	AXI 2826/10 GOLD LINE	AXI 2826/10 GOLD LINE V2
Battery	3 - 5 Li-Poly	3 - 5 Li-Poly
RPM/V	920	920
Max. efficiency	84%	86%
Max. efficiency current	20 - 30 A (>78%)	20 - 30 A (>78%)
No load current	1.7 A	1.7 A
Current capacity	42 A/60 s	43 A/60 s
Internal Resistance	42 mohm	20 mohm
Dimensions (D x L)	35x48 mm	35x52 mm
Shaft diameter	5 mm	5 mm
Weight	181 g	177 g
Max. Power	723 W	740 W

Table 3.1: AXI 2826/10 GOLD LINE and AXI 2826/10 GOLD LINE V2 specifications [26].

Right off the top, the V2 has a 2% more maximum efficiency, that although is not very relevant for the goal of this study, shows that the construction of the motor has been upgraded. It can now handle 1 more Ampere of maximum current, increasing the maximum power to 740W. The internal resistance has also been reduced by more than 50% and thermal properties have been enhanced, which is important because field weakening may heat up the motor. With all these improvements, plus a reduction in weight, the V2 appears to be a better choice, and the tests were conducted with it.

The BEMF of the ACC motor was measured using an oscilloscope. It can be observed in Figure 3.2 that the BEMF of this motor has a more sinusoidal shape, rather than trapezoidal. The measured BEMF is represented in blue, and a sinusoidal wave was added in a yellow dashed line for comparison reasons.

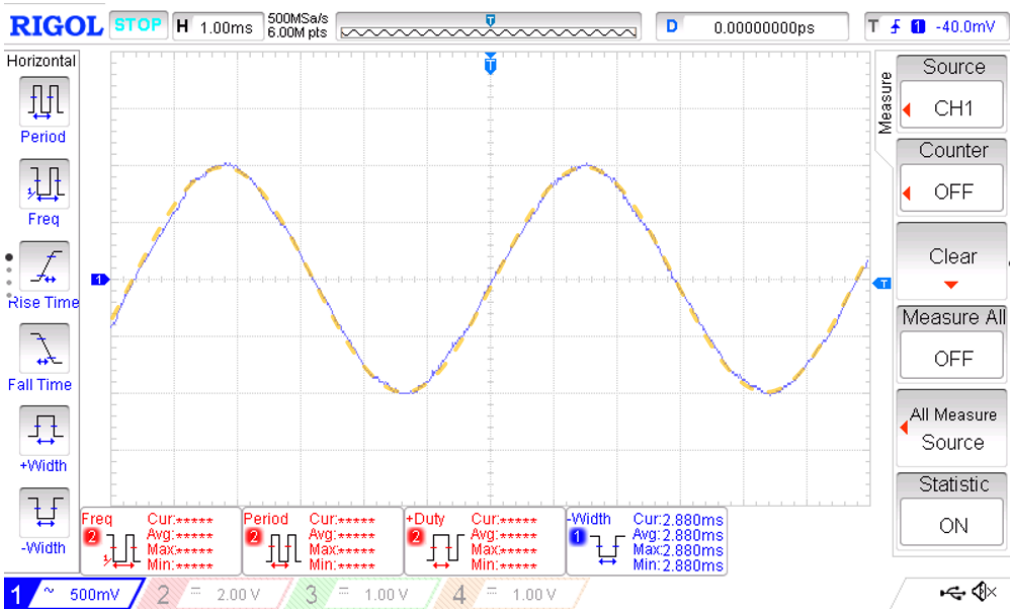

Figure 3.2: Measured BEMF of the ACC motor (in blue).

3.2 Electronic Speed Controllers

When it comes to the ESCs, 2 of them were used. One was the Castle Creations Phoenix ICE 75 (CL PI 75), which uses sensorless trapezoidal commutation to drive the motor, and the other one was an A50s by Team Triforce UK, which runs VESC software and supports field-oriented control, and, more recently, field weakening. A picture of both is shown in Figure 3.3.

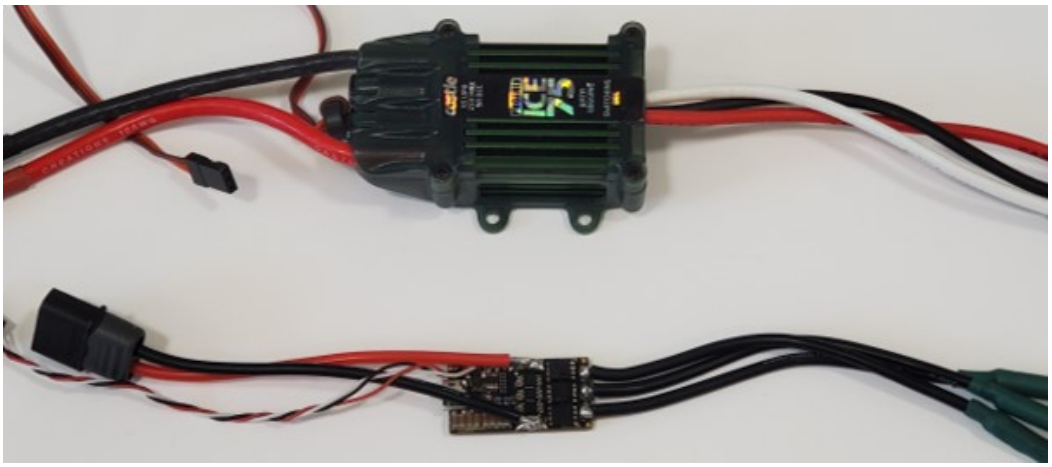

Figure 3.3: On top: Castle Creations Phoenix ICE 75, on bottom: Team Triforce UK A50S

Characteristics of the Castle Creations Phoenix ICE 75 include:

- Current Rating: 75 A;
- Voltage Rating: Li-Po 1S - 8S and Ni-Cd/Ni-MH 1S-22S;
- Mass with wires: 99 g;
- Dimensions without wires: 66 x 33 x 22.9 mm^3;
- Selectable BEC: 5 A max, 5-7 V (in increments of 0.1 V);

This ESC was selected to represent the trapezoidal strategy, due to Castle Link being a reputable brand that produces high quality ESCs.

Characteristics of the Triforce A50S include:

- Current Rating: 23 A with no airflow, 35 A with light airflow, 50 A burst;
- Voltage Rating: Li-Po 2S - 6S;
- Mass with wires: 19 g;
- Dimensions without wires: 34.2 x 17.9 x 5.5 mm^3;
- BEC: 5 V, max 0.4 A;

This ESC was selected to represent the FOC strategy because it supported VESC software and

field weakening, and is much smaller compared to similar devices.

Between the chosen ESCs, the size difference is significant and has great impact on the cooling of the ESC. The Phoenix ICE 75 has its size mainly because of the included heat sink. The Triforce A50S lacks this heat sink, which made it heat up quite a bit when field weakening was enabled. The solution implemented in the static and dynamics tests were different and are discussed in the sections 3.3 and 3.4. A more definitive solution is presented in chapter 5.

To switch efficiently between ESCs, bullet connectors were soldered to the ESC and motor leads, as well as XT60 connectors for connection with the power supply. Figure 3.4 shows the connection diagram of the components.

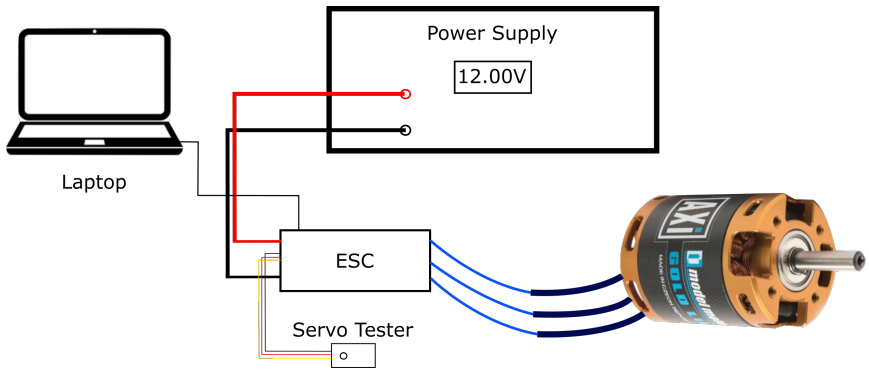

Figure 3.4: Connection diagram of the static test setup.

3.2.1 Castle Creations Phoenix ICE 75

In order to connect this ESC to a computer, a Castle Link adapter and the Castle Link software are needed. All the options in the program are presented in drop down menus along with their meanings, which are thoroughly explained and make it very simple to use.

The settings that were changed in this study to see its impact on performance were Motor Timing and PWM Rate (see Figure 3.5).

In Motor Timing Advance three options are provided: Low, Normal and High. This setting changes the timing advance range used on the motor. In other words, it is going to send current to the motor earlier or later, depending on the chosen option, which makes the motor receive the current more or less in phase with the its BEMF. If the current is in phase with the BEMF, all current will be used for torque production, the motor will be more efficient and no field weakening will take place. Normally, the Low setting is slightly more efficient and provides less power, while the High setting makes the current advance in relation to the back electromotive force, thus providing some field weakening, so it is slightly less efficient and provides more power.

Changing the PWM Rate changes the frequency at which the ESC sends commands to the motor. In theory, using higher frequencies, the motor RPM can be controlled more accurately but it also increases the temperature of the controller.

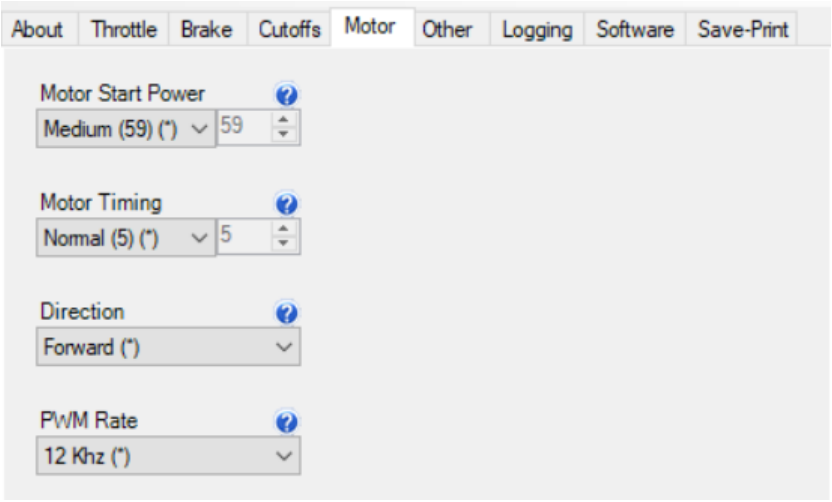

Figure 3.5: Screenshot of Castle Link showing some the settings that were changed in this study.

3.2.2 Triforce A50S

In order to connect the Triforce A50S ESC to the computer, a USB to micro USB cable is needed and the ESC must be powered externally. VESC Tool [27] must also be installed on the computer.

VESC Tool is a feature packed software that works with VESC ESCs such as the Triforce A50S. The software allows to upload firmware to the ESC, monitor and control a large a number of settings such as temperature, voltage, current and RPM ranges, PID control, position sensing, commutation modes, etc. It can also receive real-time data from the ESC or conduct automated runs.

To begin using the program, the connection to the ESC must be made by clicking on Auto-Connect (see number 1 in Figure 3.6). If the motor and ESC combination is being used for the first time, the “Setup Motors FOC” (see number 2 in Figure 3.6) wizard should be ran, so that the ESC can detect the following motor parameters: Motor Resistance (R) in Ohm [Ω], Motor Inductance (L) in Henry [H] and Motor Flux Linkage (λ) in Weber [Wb].

Next, the FOC optimization on the bottom of the FOC page should be ran in order to optimize the motor control.

At this point, the motor is ready to spin. Manual adjustments to settings such as maximum motor currents, maximum battery currents, RPM limits, etc. may be made if needed. Whenever making any changes, the ”write motor configuration” (shown in Figure 3.6) button on the right side toolbar has to be clicked so that the information is sent to the ESC. Similarly,

the ”read motor configuration” (see Figure 3.6) button can be used to read what information is written on the ESC.

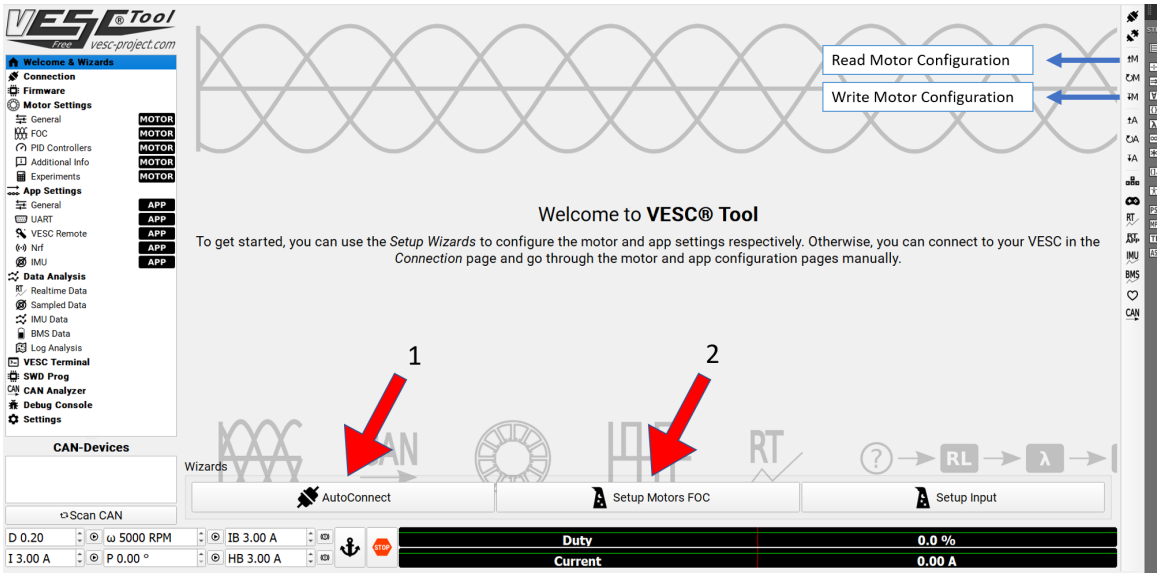

Figure 3.6: Screenshot showing the welcome page, the AutoConnect button and the Setup Motors FOC button.

For this study the switching frequency was first changed, but the motor would not run as smoothly as in the default 25 kHz value, so the changes were reverted and the frequency remained the same throughout the experiments.

The parameter changed next was the one responsible for field weakening. In this tool, it is presented as a ”Motor Inductance Difference ($Ld - Lq$)” [µH] (see Figure 3.7). In order to have this option, the ESC must be updated to the latest firmware, which was provided by Team Triforce following our e-mail request. The difference between Ld and Lq inductance represents the motor saliency. A value different from zero will enable field weakening, which will gradually inject negative current in the field axis as throttle increases, weakening the magnets of the motor.

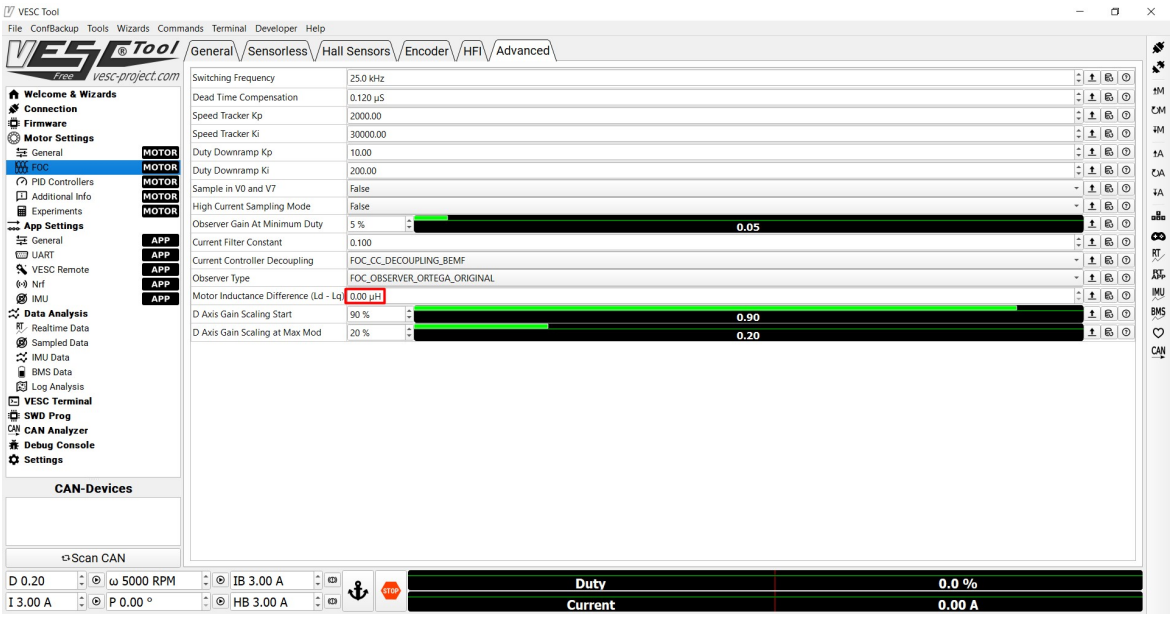

Figure 3.7: Screenshot of the VESC Tool, on the page where Field Weakening may be enabled (in the red box).

3.3 Static Tests

Static tests provide an insight on the behaviour of the chosen setup on the ground, where there is little to none relative wind. The static tests were conducted in the Faculty of Engineering of University of Beira Interior. A diagram of the static thrust measuring stand setup is shown in Figure 3.8.

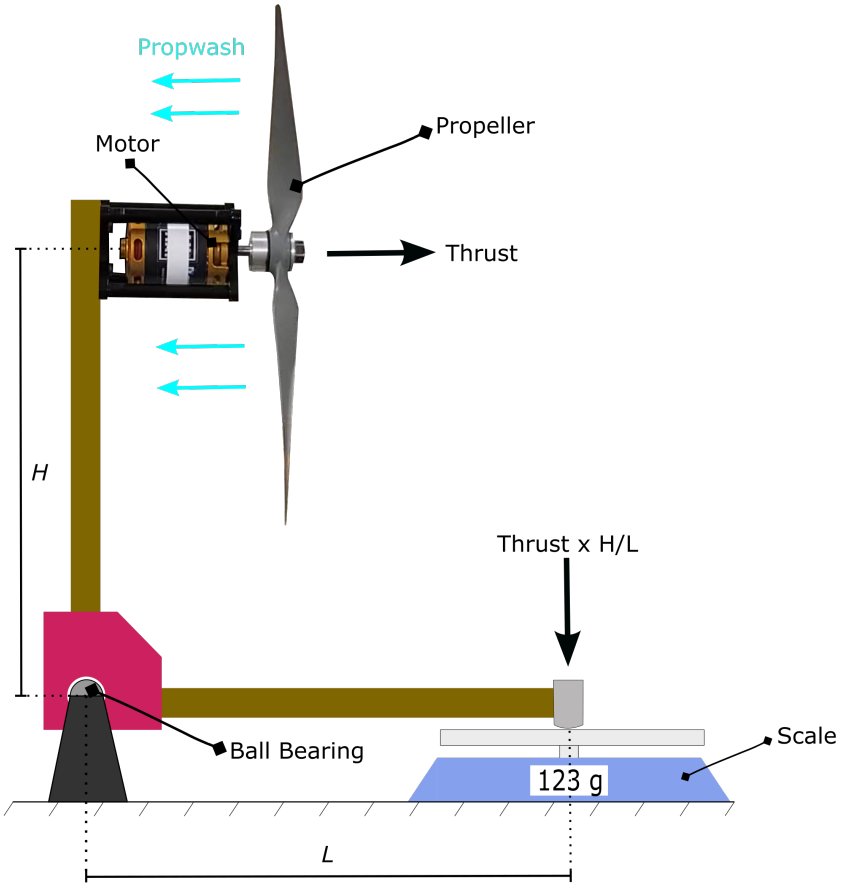

Figure 3.8: Diagram of the static thrust measuring stand setup.

A rocker made of two wooden levers at a 90º angle, connected with 3D printed pieces and ball bearings make it possible to transfer the thrust produced by the propeller to the scale. Although the wooden poles have the same length, the important measurements to take into consideration are the distance from the ball bearing axis to the motor and propeller axis (represented by H in Figure 3.8) and the distance from the ball bearing axis to the touching point in the scale (represented by L in Figure 3.8). In this case, H was 22.5 cm, and L was 24 cm. So in order to obtain the correct values, the value read on the scale was multiplied by L/H.

A picture of the implemented setup is shown in Figure 3.9.

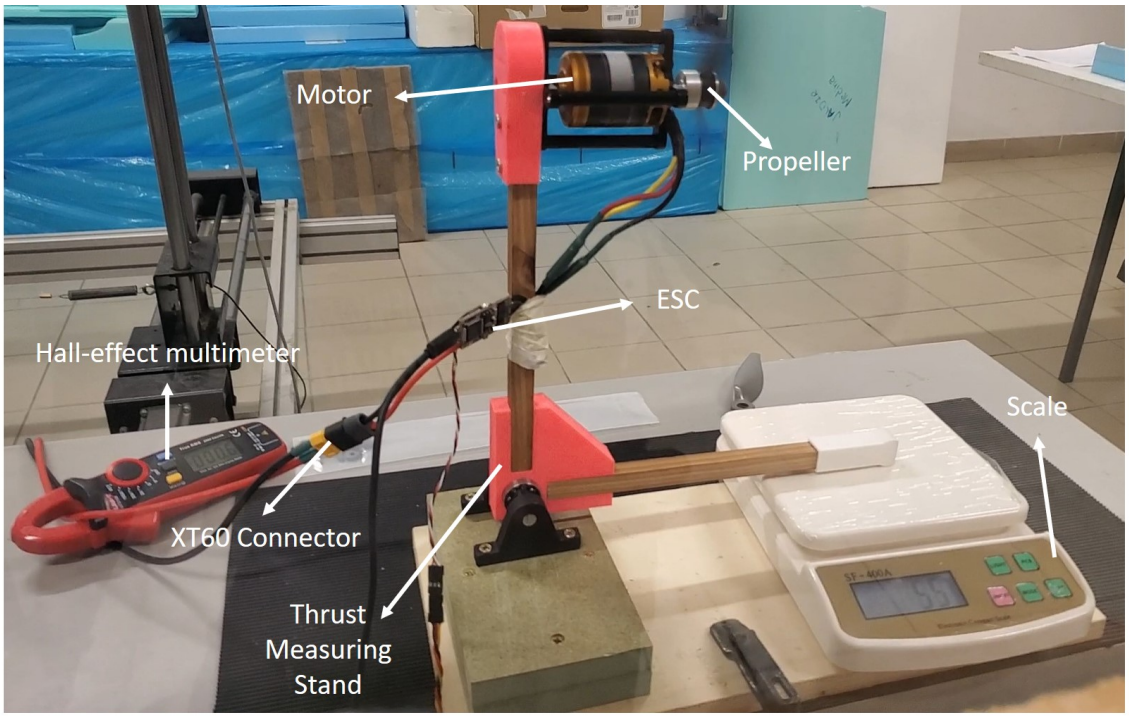

Figure 3.9: Picture of the static thrust measuring stand setup.

The ESC and motor were powered with a power supply set to 12.00 V and a current rating of up to 60 A. The voltage was set to 12.00 V because it is representative of the battery of the aircraft in the take-off stage of the Air Cargo Challenge. A multimeter with a Hall effect clamp and a precision of 0.1 A was used to measure the current and a SF-400A kitchen scale with a precision of 1 g was used to measure the thrust. It is important to note that when enabling field weakening, the Trifoce A50S heated pretty fast, so it was mounted in the prop wash of the propeller in order to keep it at a safe temperature (as seen in Figure 3.9)

It is also important to keep in mind not to use cables that are too long from the power supply to the ESC, because their inductance increases with length and this was the reason why on the first static tests the ESC would shut down at high currents.

3.3.1 Testing Conditions

Each test consisted of an incremental increase of throttle from roughly 10% to 100%. The Triforce A50S was controlled directly from the computer via the VESC Tool. So, it was possible to know at what throttle percentage it was at all times. Since the Phoenix ICE 75 did not have this feature and it was being controlled with a servo tester, the throttle was gradually increased and after each run, the ESC log file was read to know the exact throttle percentage that corresponded to each thrust and current values.

With the Phoenix ICE 75, 9 tests were conducted with each propeller, corresponding to 9 different combinations of PWM Rate and Motor Timing, as shown in Figure 3.10.

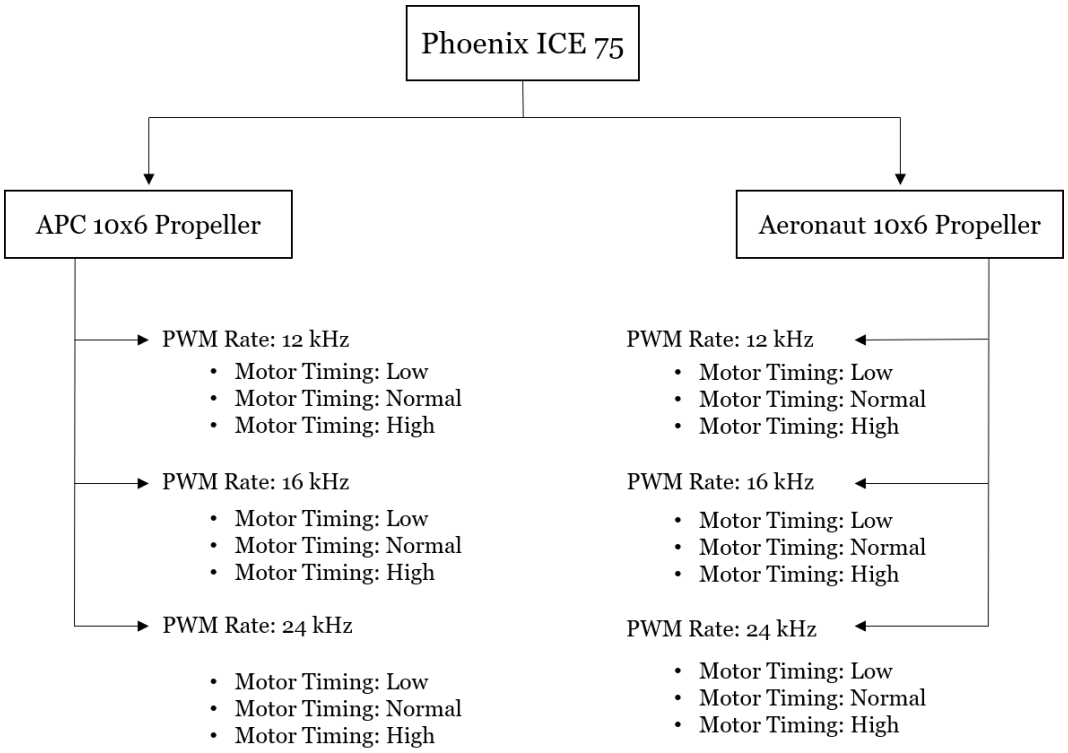

Figure 3.10: Static tests performed with the Phoenix ICE 75 ESC.

With the Triforce A50S, 4 tests with each propeller were performed, corresponding to different magnitudes of field weakening, as shown in Figure 3.11.

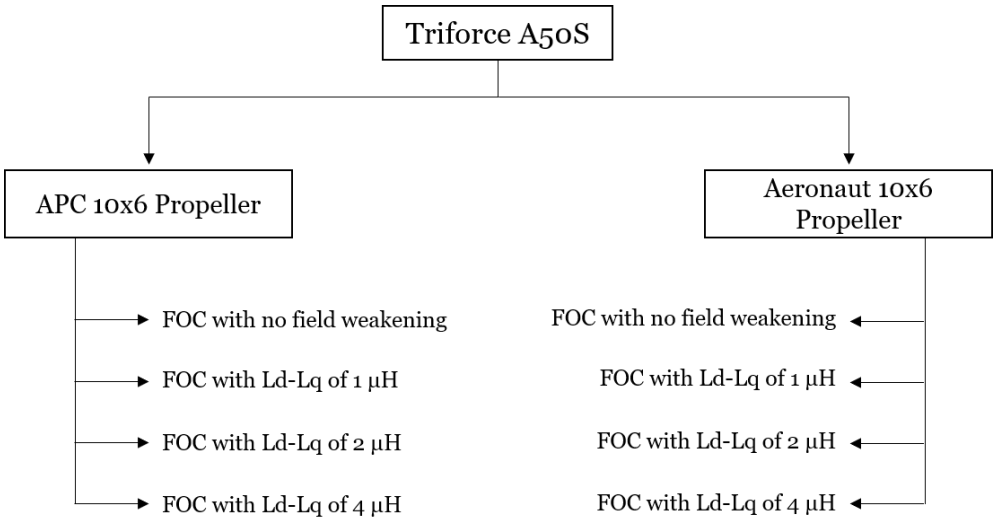

Figure 3.11: Static tests performed with the Triforce A50S ESC.

This resulted in 26 different testing conditions for the static experiments. The results are shown in Section 1 of Chapter 4.

3.4 Wind Tunnel Tests

Wind tunnel tests provide an overview of how the chosen setup behaves in flight, where there is relative wind.

The main wind tunnel in University of Beira Interior was used. Its installation is thoroughly documented in [28]. A general scheme is shown in Figure 3.12.

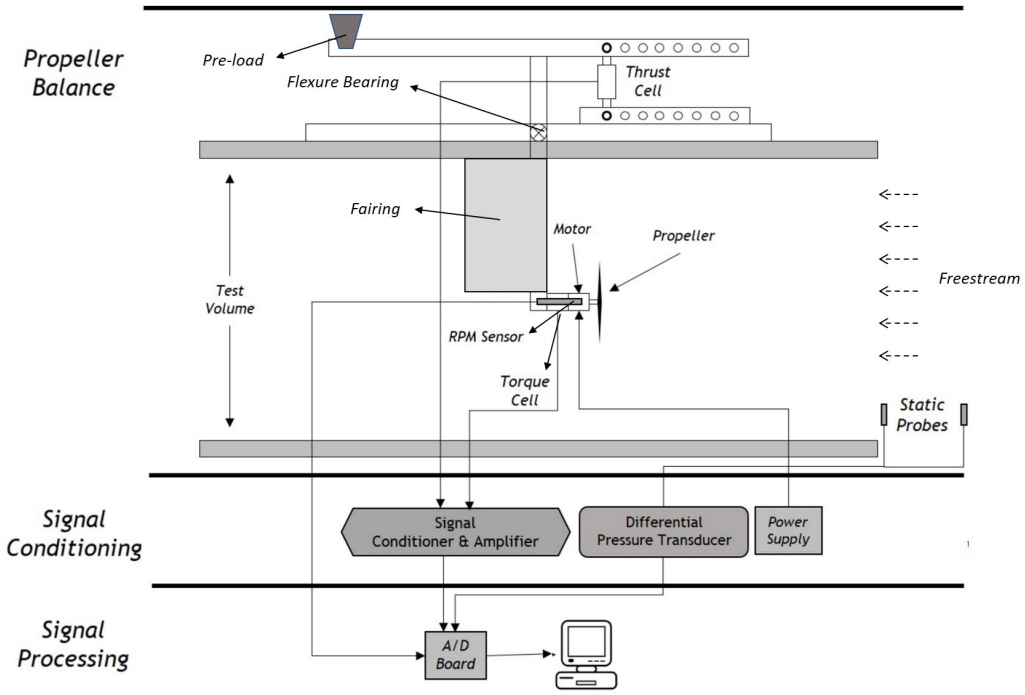

Figure 3.12: Measurement System Schematic Overview (adapted from [28]).

This tunnel is equipped with various equipment such as an RPM Sensor that outputs the RPM of the motor, a torque cell used to measure the torque generated by the motor, and a load cell to measure how much thrust is generated. The freestream velocity is measured with a differential pressure transducer, an absolute pressure transducer and a thermocouple. A mast fairing is also installed over the wiring and motor fixation structure to make it more aerodynamic. A pre-load is placed on the opposite side of the load cell responsible for measuring thrust, in order to keep it in tension even during negative thrust conditions.

Figure 3.13 shows a picture of the installation.

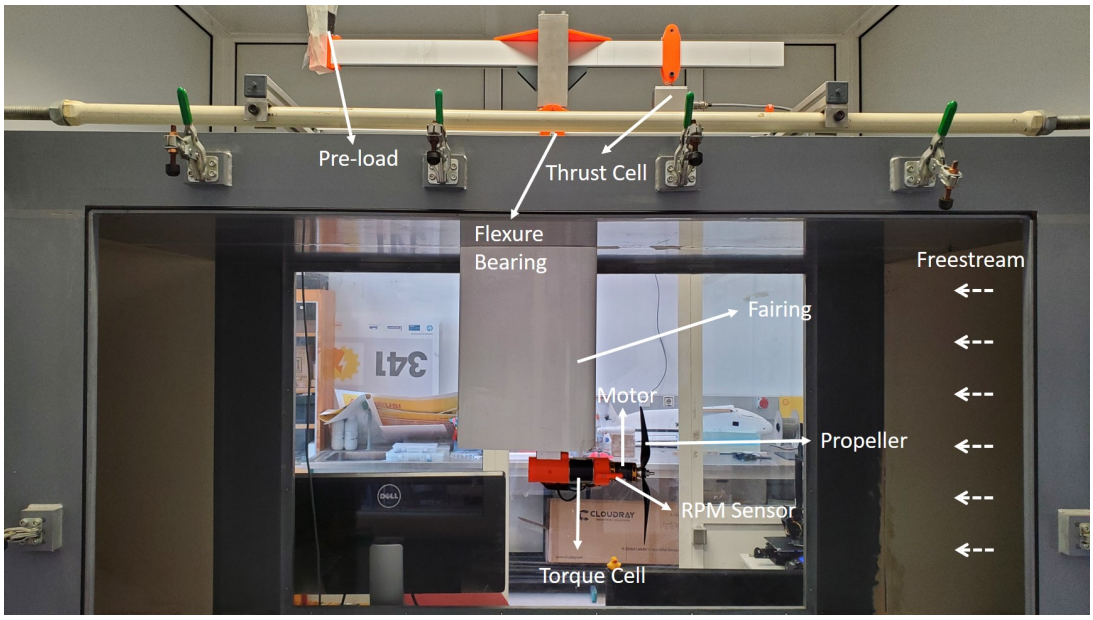

Figure 3.13: Picture of the wind tunnel setup mounted with the Aeronaut 10x6 propeller.

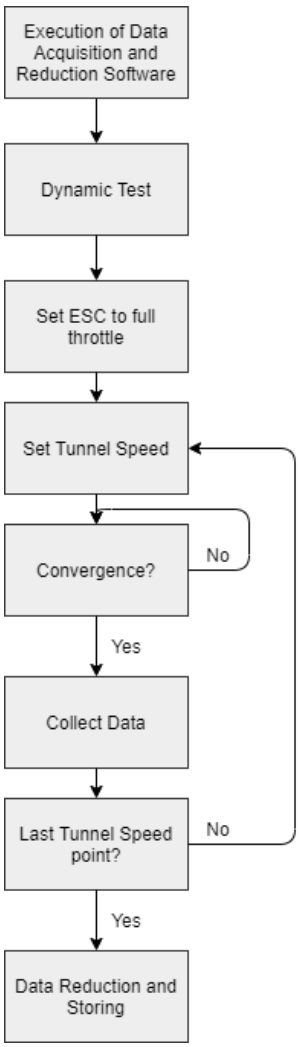

Figure 3.14: Flowchart of the test methodology used in the wind tunnel.

The tunnel is equipped with its own ESC that is directly connected to the LabView software on the computer and it is usually used to test motors and propeller. As it was needed to use different ESCs, the tunnel ESC was disconnected, thus losing the motor connection to the LabView software, which is not relevant since the tests were performed at full throttle. The procedure is described in the flowchart in Figure 3.14.

Before starting the experiments, full calibration of the torque sensor, the load cell and pressure sensors were made. Every test was performed at open throttle and with an incremental increase of the wind speed, starting at 5 m/s and up to a maximum of 32 m/s, depending on how much thrust was being generated, so that windmill break state would be avoided. At each wind speed, and after convergence, a 200 point average of the measured values was calculated and stored automatically by the LabView software.

The uncertainties of the primary measurement sensors are displayed in Table 3.2. The uncertainty of the measured results is shown in subsection 4.2.5 and was calculated using the methodology described in reference [29].

Measurement	**Sensor**	**Uncertainty**
Thrust, T	FGP FN3148	$\Delta T = \pm 0.05N$
Torque, Q	Transducer Techniques RTS-100	$\Delta Q = \pm 0.000339N.m$
Atmospheric Temperature, T_{atm}	National Instruments LM335	$\Delta T_{atm} = \pm 1.0K$
Atmospheric Pressure, P_{atm}	Freescale Semiconductor MPXA4115A	$\Delta P_{atm} = \pm 30.0Pa$
Propeller Rotation Speed, n	Fairchild Semiconductor QRD1114	$\Delta RPM = \pm 5RPM$
Static Ports Differential Pressure, $(p_1 - p_2)$	MKS 226A	$\Delta(p_1 - p_2) = \pm 0.003xReading$

Table 3.2: Uncertainties of the primary measurement sensors.

The measured values are: thrust (T), torque (Q), freestream velocity (V), revolutions per second (n), voltage (v), current (I), static pressure (P_s), atmospheric pressure (P_{atm}) and air temperature (T_{atm}).

From these quantities, the air density ρ can be computed:

$$\rho = \frac{P_{atm}}{RT_{atm}} \tag{3.1}$$

Advance ratio, J, can be calculated with V, n and the propeller diameter, D:

$$J = \frac{V}{nD} \tag{3.2}$$

Thrust coefficient, C_T, and power coefficient, C_P are calculated with the respective parameters T and power, $P = 2\pi nQ$.

$$C_T = \frac{T}{\rho n^2 D^4} \tag{3.3}$$

$$C_P = \frac{P}{\rho n^3 D^5} \tag{3.4}$$

$Thrust/Current$ was calculated and used as the propulsive efficiency of the propeller.

Similarly to the static tests, there was a need to keep the Triforce A50S cool when enabling field weakening. In this case, since the ESC was mounted on top of the tunnel, and placing it behind the propeller would not be as straightforward as in the static tests, compressed air was blown at the ESC, keeping it at a safe temperature.

3.4.1 Testing Conditions

From the static tests, it was observed that changing the PWM Rate of the Phoenix ICE 75 had no significant impact on the generated thrust so, for the wind tunnel tests, the PWM Rate was kept at its default value of 12 kHz.

The tests shown in Figure 3.15 were performed.

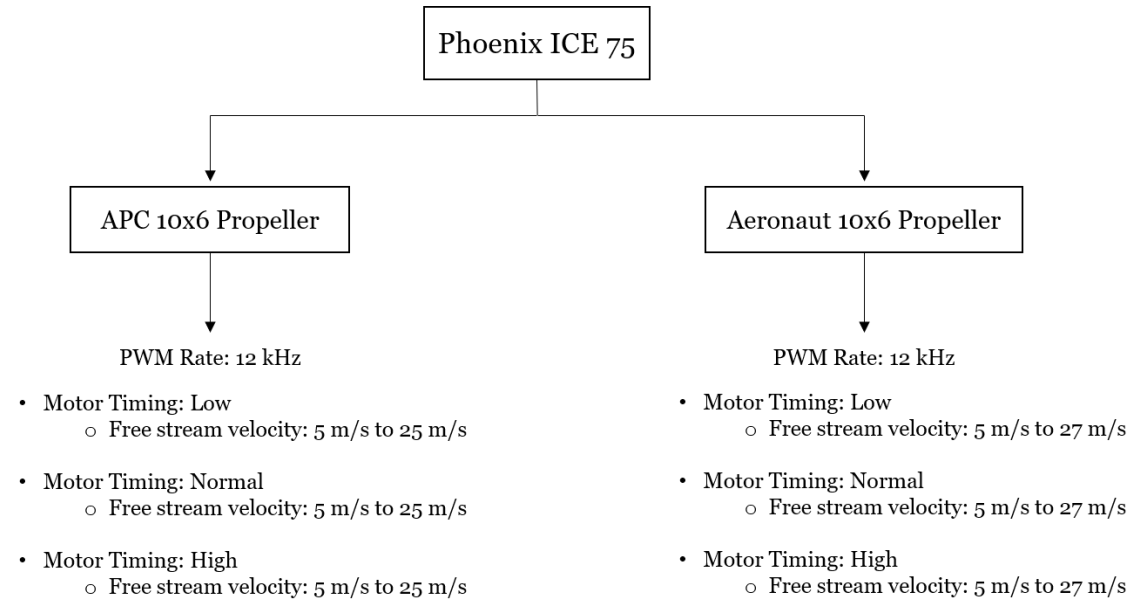

Figure 3.15: Dynamic tests performed with the Phoenix ICE 75 ESC

At this point, it was clear that the Aeronaut propeller generated more thrust than the APC propeller, so the tests with the Triforce A50S ESC, shown in Figure 3.16, were only conducted with the Aeronaut propeller.

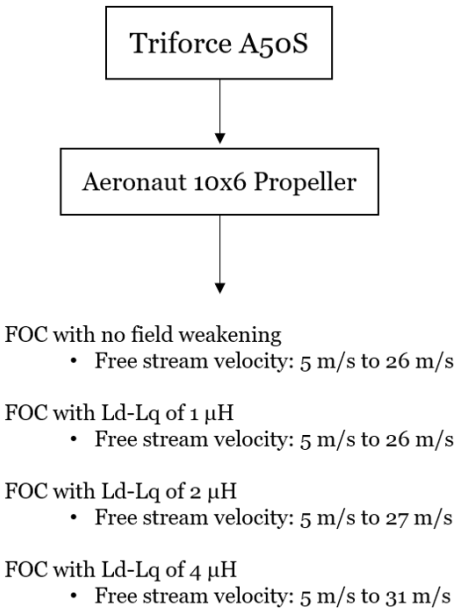

Figure 3.16: Dynamic tests performed with the Triforce A50S ESC.

This resulted in 10 different testing conditions for the wind tunnel experiments. The results are presented in Section 2 of Chapter 4.

Chapter 4

Results and Discussion

4.1 Static Tests

4.1.1 Propeller

The thrust generated and current drawn by each of the tested propellers as the duty cycle is ramped up are shown in Figures 4.1 and 4.2. Figure 4.1 shows these results with the Phoenix Ice 75 ESC with PWM Rate of 12 kHz and Motor Timing set to High. It can be seen that up to around 60% duty cycle there is no noticeable difference between the two propellers, but from 60% to 100% duty cycle the Aeronaut propeller produces more thrust and draws more current than the APC propeller. At 100% duty cycle, the difference in thrust and current is 0.39 N and 2.60 A, corresponding to 3.0% and 11.8%, respectively, which means that the APC propeller provides more thrust per Ampere of current. At this duty cycle, the APC propeller is generating 0.59 N/A, while the Aeronaut propeller is generating 0.54 N/A, which is 8.5% less than the APC propeller. It can also be observed that below 60% duty cycle the thrust increment is nearly linear, while above 60% it becomes exponential.

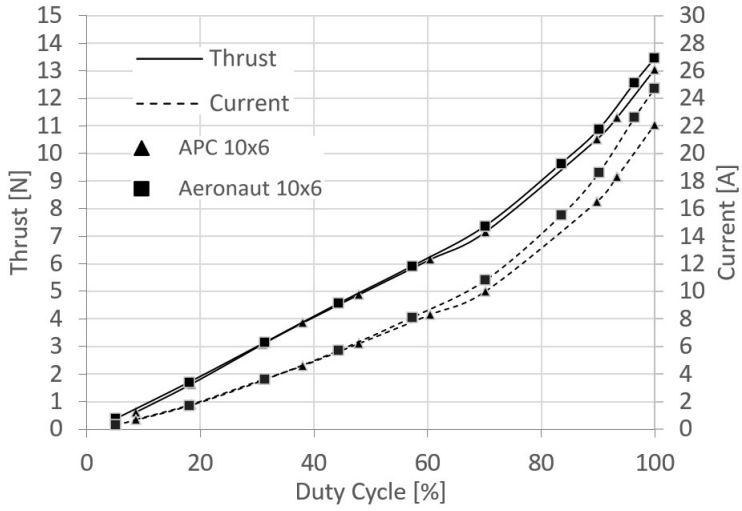

Figure 4.1: Thrust and current as functions of duty cycle for both propellers using the Phoenix ICE 75 ESC with 12 kHz PWM Rate and High Motor Timing.

Figure 4.2 shows the same data, but using the Triforce A50S ESC with FOC and no field weakening. Here, the Aeronaut propeller also generates more thrust and draws more current, but the difference starts to get visible near the lower values of duty cycle. At 100% duty cycle, the difference in thrust and current is 0.53 N and 3.90 A, corresponding to 4.0% and 15.6%,

respectively. At this duty cycle, the APC propeller is generating 0.54 N/A, while the Aeronaut propeller is generating 0.49 N/A, which corresponds to 9.3% less than the APC propeller. It can also be observed that the thrust increment is exponential from the start.

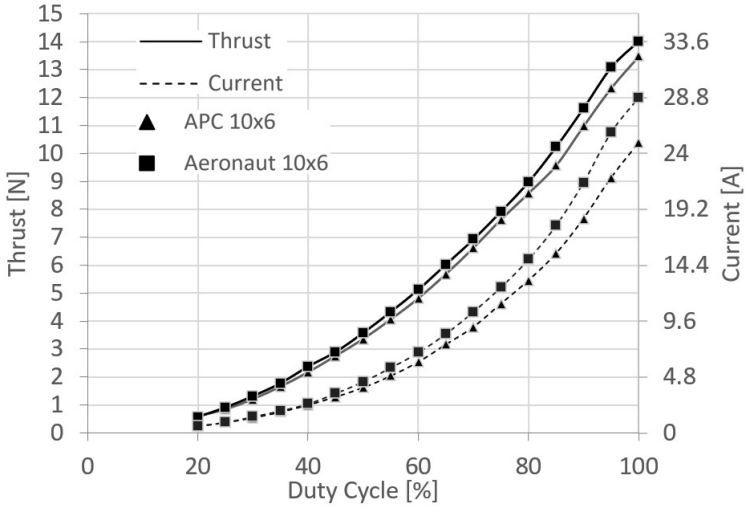

Figure 4.2: Thrust and current as functions of duty cycle for both propellers using the Triforce A50S ESC with FOC and no field weakening.

4.1.2 Trapezoidal - PWM Rate

Figure 4.3 shows the thrust and current results as functions of duty cycle of the Aeronaut propeller with the Phoenix ICE 75 ESC running on Low timing for 3 different PWM Rates: 12kHz, 16kHz and 24kHz. It can be observed that the PWM affects thrust and current mainly between 0% and 75% duty cycle, and makes virtually no difference at higher values of duty cycle. The same graphs for Normal and High Timing provide similar information, so they were omitted from the present document.

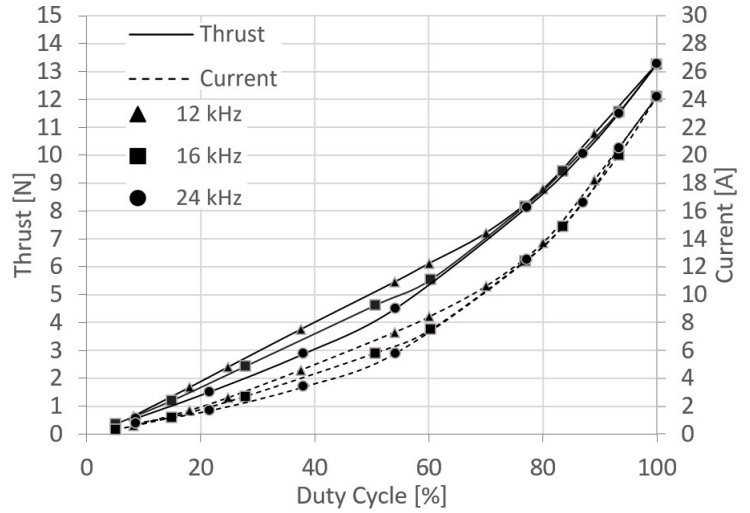

Figure 4.3: Thrust and current as functions of duty cycle for the Phoenix ICE 75 ESC on Low Timing using the Aeronaut propeller.

4.1.3 Trapezoidal - Motor Timing

Figure 4.4 shows the thrust and current results as functions of duty cycle for the Aeronaut propeller and the Phoenix ICE 75 ESC with the PWM Rate fixed at the default 12 kHz and the different motor timings: Low, Normal and High. It can be observed that there is no significant variation in thrust and current values. There is a 1-3% increase in the thrust and current values at 100% duty cycle between the Low and High setting, depending on the setup.

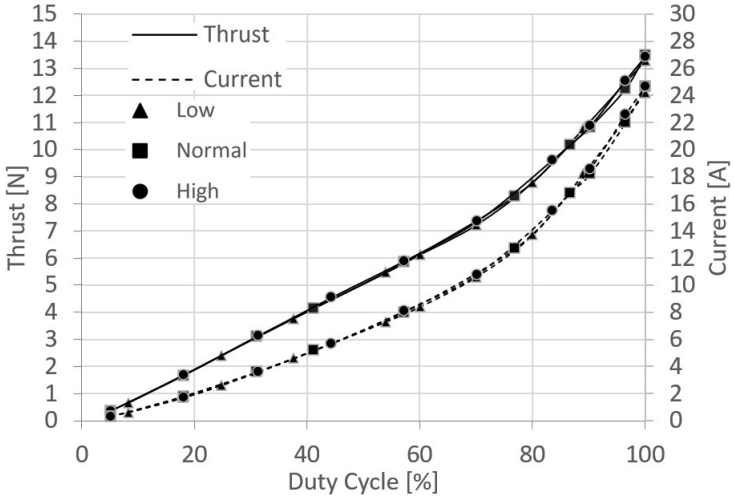

Figure 4.4: Thrust and current as functions of duty cycle for different ESC timing settings, using the Phoenix ICE 75 ESC at 12 kHz PWM Rate and the Aeronaut propeller.

4.1.4 FOC and field weakening

Figure 4.5 shows the thrust generated and current consumed as functions of the duty cycle for the Aeronaut propeller and the Triforce A50S ESC with FOC, starting without field weakening and gradually increasing the $Ld - Lq$ value up to 4 µH. As this value is increased, the increase in thrust is notable, as well as the increase in drawn current. At full throttle, the thrust and current increase from the option without field weakening to the option with $Ld - Lq$ of 4 µH is 1.25 N and 7.50 A, corresponding to 8.9% and 26.0%, respectively. In terms of static thrust efficiency, the same options have values of 0.49 N/A and 0.42 N/A, respectively. The decrease in efficiency corresponds to 13.6%.

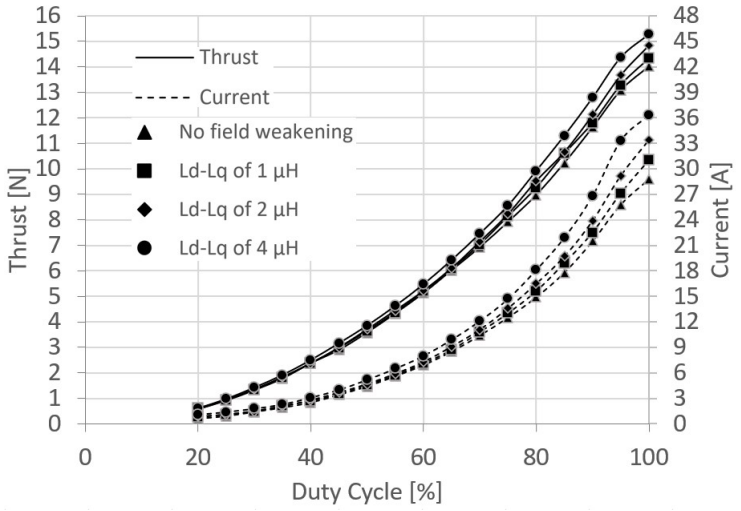

Figure 4.5: Thrust and current as functions of duty cycle for different magnitudes of field weakening, using the Triforce A50S ESC running FOC and the Aeronaut propeller.

Figure 4.6 shows the thrust and current values as functions of the duty cycle for the same configuration, but with the APC propeller. At 100% duty cycle, without field weakening, the static thrust efficiency is 0.54 N/A, while with $Ld - Lq$ of 4, this value is 0.46 N/A, corresponding to a 14.2% decrease in efficiency. Although the APC propeller generates less thrust, it does it more efficiently than the Aeronaut propeller, thus producing more thrust per unit of current.

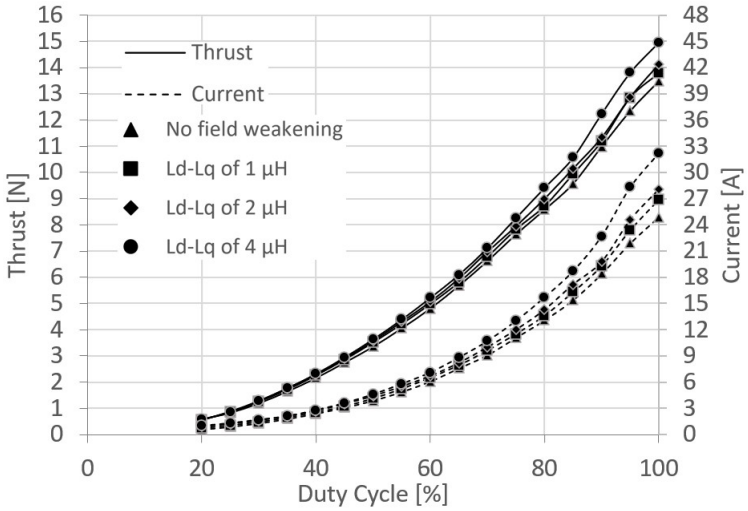

Figure 4.6: Thrust and current as functions of duty cycle for different magnitudes of field weakening, using the Triforce A50S ESC running FOC and the APC propeller.

4.1.5 Trapezoidal *versus* FOC

Figure 4.7 shows the values of thrust and current as functions of duty cycle with the Aeronaut propeller, for the various control methods: trapezoidal control on the Phoenix ICE 75 ESC (16 kHz PWM Rate and Motor Timing High, because this combination had a slightly higher thrust value at 100% than the others); FOC on the Triforce A50S ESC without field

weakening, and also FOC with the maximum tested magnitude of field weakening: $Ld - Lq$ = 4 µH.

The Phoenix ICE 75 ESC appears to have a more linear speed control and generates more thrust up to 60% duty cycle, but is caught up by the two configurations of the Triforce A50S between 60% and 75% duty cycle. The difference in thrust and current at maximum duty cycle between the Phoenix ICE 75 and the Triforce A50S with FOC and no field weakening is 0.42 N and 3.80 A, corresponding to 3.1% and 15.2%, respectively. Between FOC without field weakening and FOC with $Ld - Lq$ = 4 µH, this difference is 1.67 N and 11.30 A, corresponding to 12.3% and 45.2%. In terms of static thrust efficiency at 100% duty cycle, the Phoenix ICE 75 produces 0.54 N/A, the Triforce A50S with FOC and no field weakening produces 0.49 N/A, and the Triforce A50S with FOC and $Ld - Lq$ of 4 µH produces 0.42 N/A, illustrating the loss of efficiency caused by field weakening.

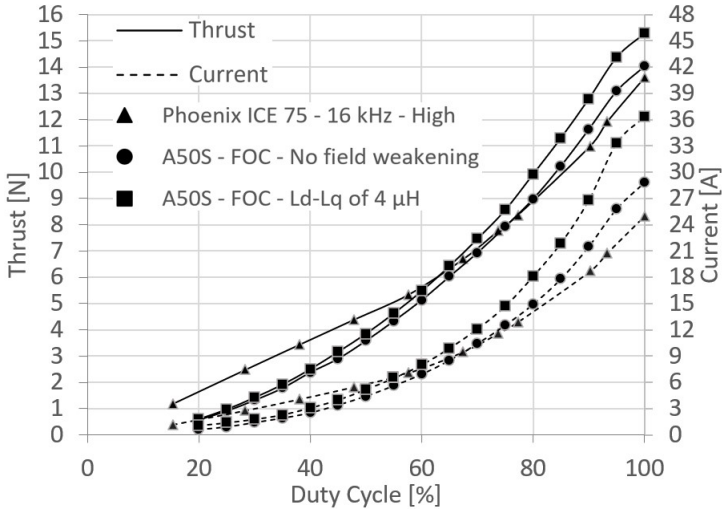

Figure 4.7: Thrust and current as functions of duty cycle for the different control strategies using the Aeronaut propeller.

4.1.6 Full Throttle Comparison

The thrust and current values at maximum duty cycle for each propeller are presented next. Figure 4.8 shows these results for the APC propeller and Figure 4.9 for the Aeronaut propeller.

The results show that the Triforce A50S ESC with FOC is able to spin the motor faster, thus offering more thrust. It can be seen that the trapezoidal control provided by the Phoenix ICE 75 generates as much as 15% less thrust than the Triforce A50S with FOC, while consuming up to 33% less current.

The Triforce A50S ESC with $Ld - Lq$ of 4 µH and the Aeronaut propeller produced the most thrust from all static tests: 15.27 N, while consuming 36.3 A. The same ESC but the APC propeller achieved 14.96 N, while consuming 32.2 A.

There was not a lot of variation in thrust with the Phoenix ICE 75 across different motor timings or PWM frequencies. In Figure 4.8 it can be seen that the maximum thrust produced with this ESC and the APC propeller was 13.05 N, while consuming 22.1 A of current, with high motor timing. The same ESC with the Aeronaut propeller (Figure 4.9) produced a maximum of 13.49 N, on normal timing, while consuming 24.7 A of current.

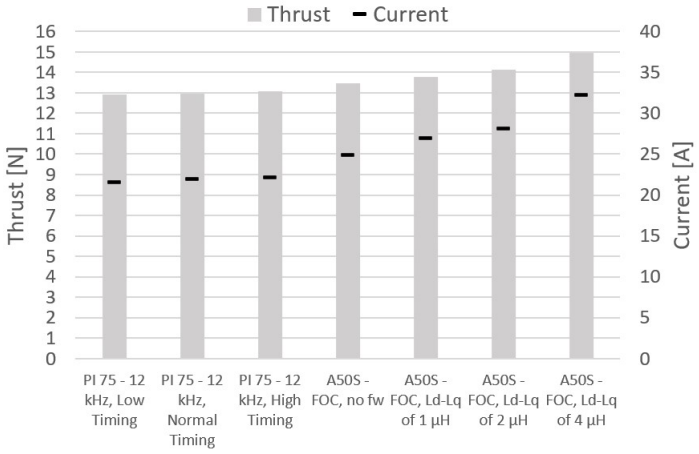

Figure 4.8: Full throttle thrust and current for different control strategies using the APC propeller.

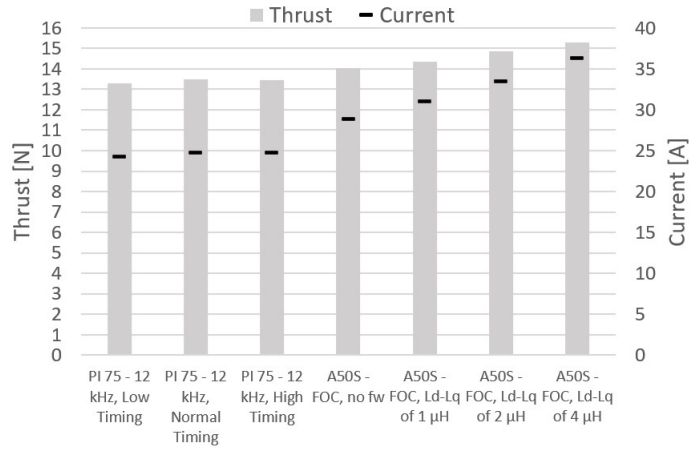

Figure 4.9: Full throttle thrust and current for different control strategies using the Aeronaut propeller.

4.1.7 Static Thrust Efficiency

Figure 4.10 shows the static thrust efficiency as function of duty cycle for both propellers, using the Phoenix ICE 75 ESC on 12 kHz PWM Rate and High Motor Timing. This shows that the APC propeller is up to 8.5% more efficient from around 50% duty cycle, even though it generates less thrust.

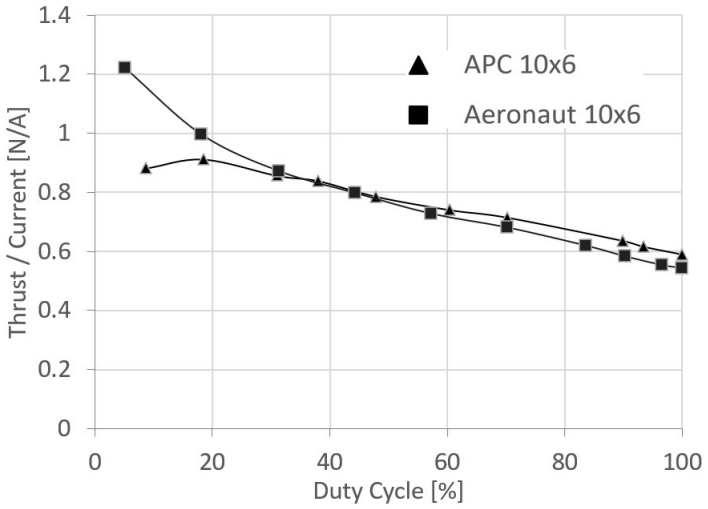

Figure 4.10: $Thrust/Current$ as function of duty cycle for both propellers using the Phoenix ICE 75 ESC on 12 kHz PWM rate and High Motor Timing.

Figure 4.11 shows the static thrust efficiency as function of the duty cycle with the Triforce A50S ESC and APC propeller for multiple magnitudes of field weakening. It is visible that, as field weakening is escalated, each Ampere generates up to 16.6% less thrust. The values until roughly 45% duty cycle are not very conclusive, because the currents at this phase are relatively small and a very small variation in measurement could affect the result of static thrust efficiency in a significant way.

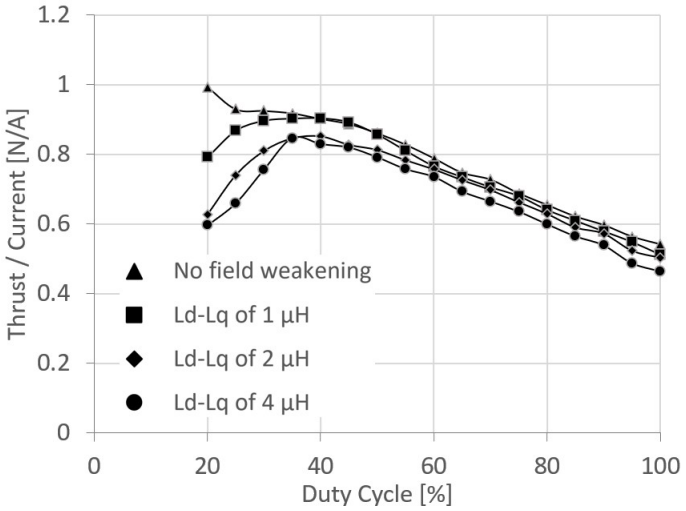

Figure 4.11: $Thrust/Current$ as function of duty cycle for different magnitudes of field weakening, with the Triforce A50S ESC running FOC and the APC propeller.

Figure 4.12 shows the static thrust efficiency of the multiple control strategies using the APC propeller. From around 75% to 100% duty cycle, the static thrust efficiency of the Phoenix ICE 75 ESC with trapezoidal commutation is the highest, followed by FOC without field weakening, and FOC with the highest tested level of field weakening ($Ld - Lq$ = 4 µH), which provides the least static thrust efficiency, as expected.

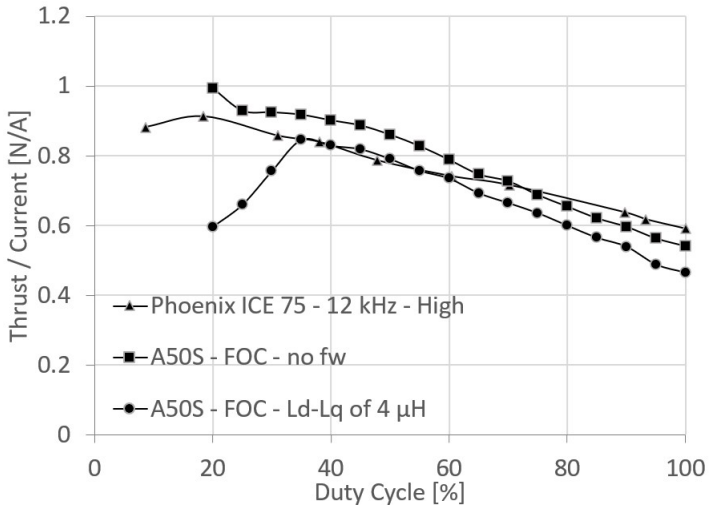

Figure 4.12: $Thrust/Current$ as function of duty cycle for different control strategies, using the APC propeller.

4.2 Wind Tunnel Tests

4.2.1 Propeller

Figure 4.13 shows the thrust generated and current drawn using the Phoenix ICE 75 ESC at 12 kHz PWM Rate, for both propellers, at full throttle, for different freestream velocities. At any freestream velocity, the Aeronaut propeller generates more thrust than the APC, and also consumes more current. For instance, at 25 m/s, the difference between the thrust and current between both propellers is 1.06 N and 1.67 A, corresponding to 22.6% and 10.7%, respectively.

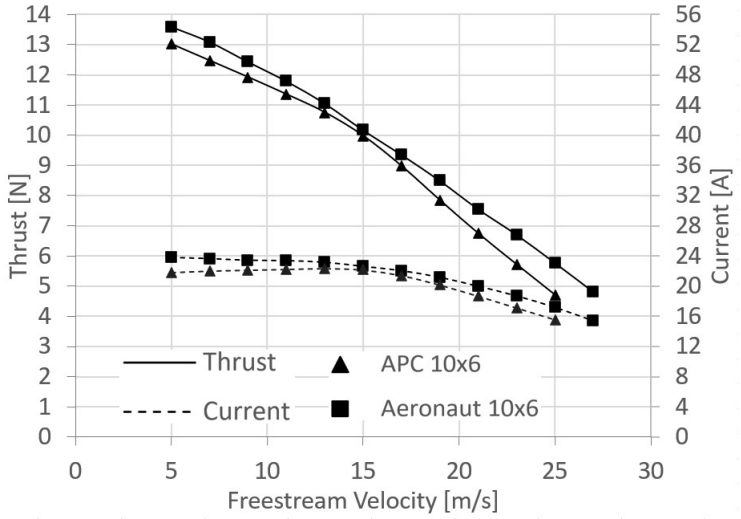

Figure 4.13: Wind tunnel full throttle thrust and current as functions of the freestream velocity for both propellers using the Phoenix ICE 75 ESC on Low Motor Timing.

To allow for a better comparison of propellers, Figure 4.14 shows the thrust coefficient, C_T, and power coefficient, C_P, as functions of advance ratio, J.

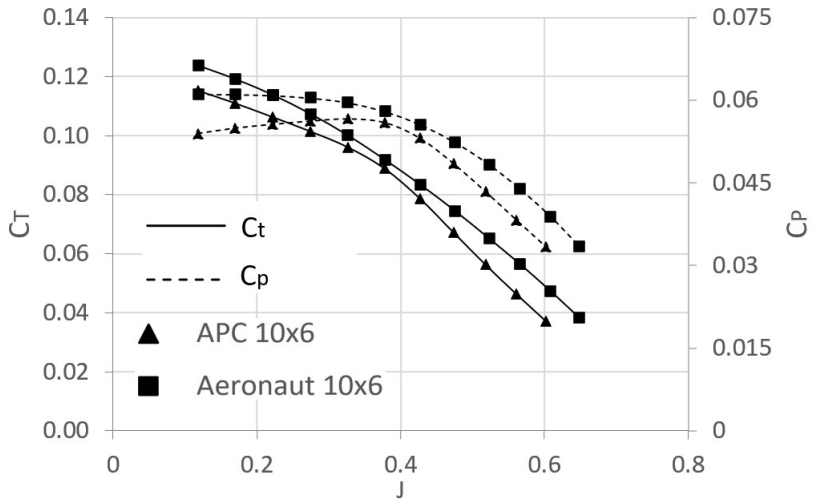

Figure 4.14: Wind tunnel full throttle thrust coefficient and power coefficient as functions of advance ratio for both propellers using the Phoenix ICE 75 on Low Motor Timing.

Figure 4.15 shows the propeller efficiency η_p as function of the advance radio, J. It can be observed that at values of advance ratio higher than 0.4, the Aeronaut propeller becomes more efficient than the APC propeller, up to 7%.

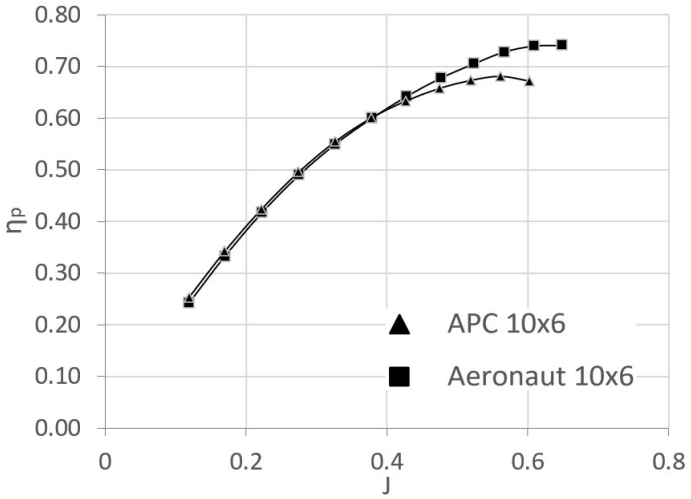

Figure 4.15: Wind tunnel full throttle propeller efficiency as function of advance ratio for both propellers using the Phoenix ICE 75 on Low Motor Timing.

Figure 4.16 shows the $Thrust/Current$ corresponding to the results of Figure 4.13. $Thrust/Current$ indicates how much thrust is each Ampere of current generating and can be interpreted as a value of the efficiency of the propulsive system. The propulsive system with the APC propeller appears to be slightly more efficient at lower freestream velocities, but is surpassed by the Aeronaut propeller at about 16 m/s freestream velocity.

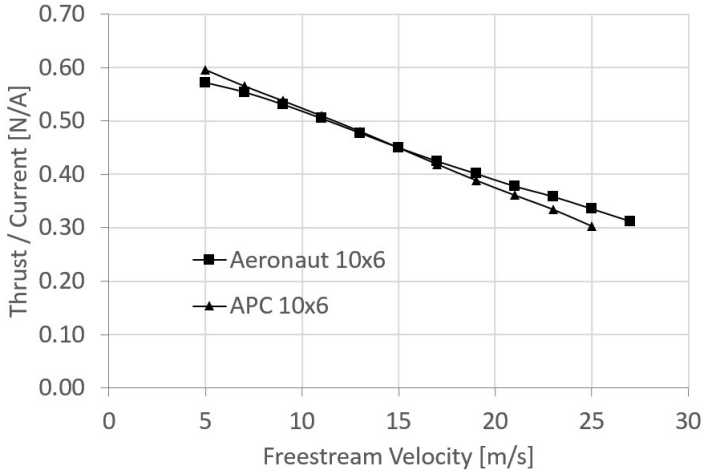

Figure 4.16: Wind tunnel full throttle $Thrust/Current$ as function of freestream velocity for both propellers using the Phoenix ICE 75 ESC on Low Motor Timing.

4.2.2 Motor Timing

Figure 4.17 shows the results of the 3 different Motor Timing options: Low, Normal and High, with the Phoenix ICE 75 ESC and using the Aeronaut propeller. At the various freestream velocities, the difference is consistent and corresponds to about 1-2%, both for thrust and current, between the Low and High setting.

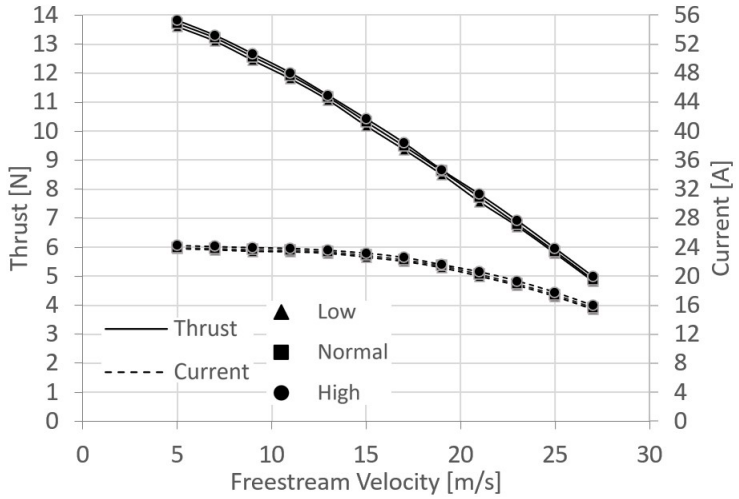

Figure 4.17: Wind tunnel full throttle thrust and current as functions of freestream velocity for the different Motor Timing options using the Phoenix ICE 75 ESC and Aeronaut propeller.

Figure 4.18 shows the $Thrust/Current$ values corresponding to the results of Figure 4.17. It can be seen that the efficiency is nearly the exact same for the different Motor Timing settings.

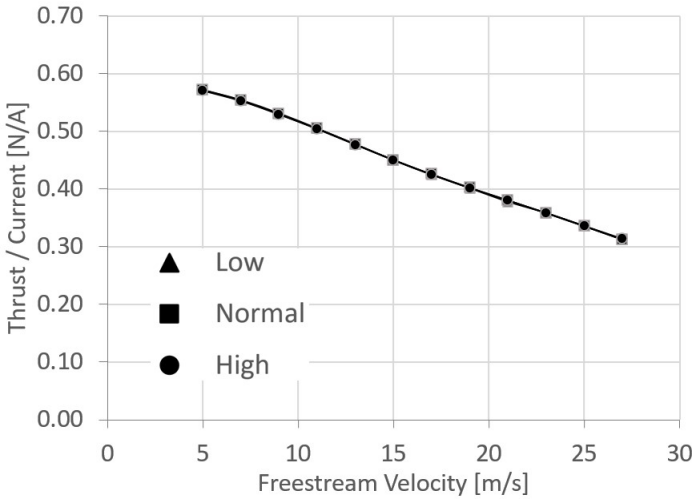

Figure 4.18: Wind tunnel full throttle $Thrust/Current$ as function of freestream velocity for the different Motor Timing options using the Phoenix ICE 75 ESC and Aeronaut propeller.

4.2.3 FOC and field weakening

Figure 4.19 shows the test results of the different field weakening magnitudes tested with the Triforce A50S ESC running FOC and the Aeronaut propeller. It can be seen that the effect of field weakening is really significant at any freestream velocity. At 5 m/s, the thrust difference between no field weakening and $Ld - Lq$ of 4 µH is about 1.2 N, and it stays roughly constant throughout the whole range of freestream velocities. As shown before, field weakening does significantly increase the drawn current. At 5 m/s, the difference between the current consumed with no field weakening and $Ld - Lq$ of 4 µH is 5.98 A, and remains roughly constant as the freestream velocity increases.

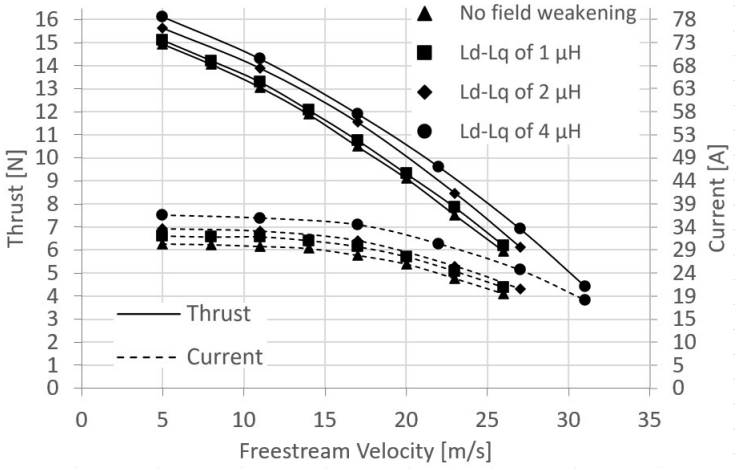

Figure 4.19: Wind tunnel full throttle thrust and current for the different magnitudes of field weakening using the Triforce A50S and Aeronaut Propeller.

Figure 4.20 shows the $Thrust/Current$ values corresponding to the results of Figure 4.19. The most efficient setup is the one without field weakening, and efficiency decreases as $Ld - Lq$ is increased. The difference in efficiency is more noticeable for lower freestream velocities,

and becomes less noticeable as freestream velocity is increased. This means that, despite the fact that the efficiency of the motor drops with more intense field weakening, the global propulsion system efficiency is unchanged as the expected Air Cargo Challenge 2022 aircraft cruise airspeed is higher than 25m/s.

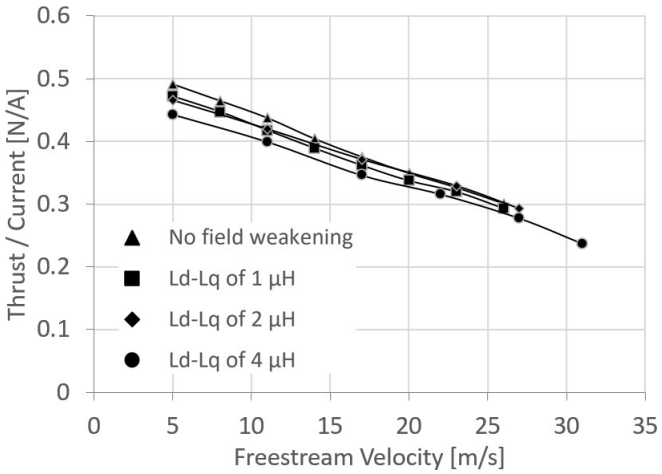

Figure 4.20: Wind tunnel full throttle $Thrust/Current$ as function of freestream velocity for the different magnitudes of field weakening, using the Triforce A50S and Aeronaut Propeller.

Figure 4.21 shows the RPM values for the same conditions, proving that the field weakening is working and the motor is able to spin faster as the value of $Ld - Lq$ is increased.

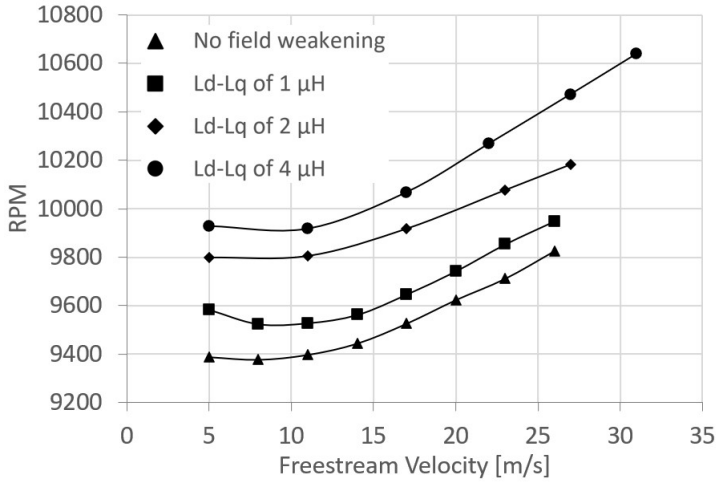

Figure 4.21: Wind tunnel full throttle RPM as function of freestream velocity for the different magnitudes of field weakening, using the Triforce A50S and Aeronaut Propeller.

4.2.4 Control Strategy Comparison

To finalize, the thrust, current, efficiency and RPM values as function of freestream velocity of all the tested combinations in the wind tunnel with the Aeronaut propeller are displayed in Figure 4.22, Figure 4.23 and Figure 4.25 , respectively.

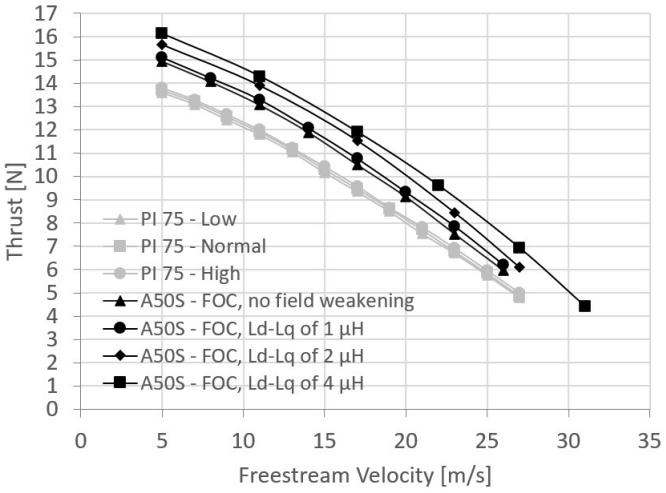

Figure 4.22: Wind tunnel full throttle thrust as function of the freestream velocity for the 7 configurations tested with the Aeronaut propeller and both ESCs.

Figure 4.22 shows that FOC produces more thrust than trapezoidal control, even without field weakening. With field weakening control, an additional 2 N of thrust can be achieved over the trapezoidal control, throughout pretty much the entire spectrum of freestream velocities.

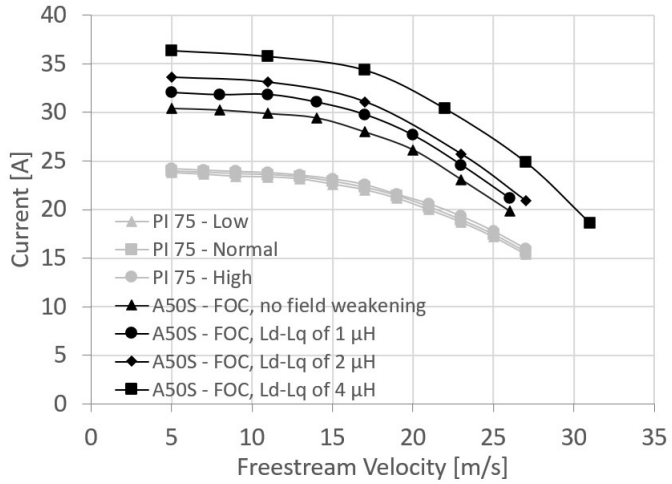

Figure 4.23: Wind tunnel full throttle current as function of freestream velocity for the 7 configurations tested with the Aeronaut propeller and both ESCs.

From figure 4.23, it can be seen that the increase of thrust from field weakening comes at the expense of an even bigger increase in current. The difference between trapezoidal control and the maximum magnitude of field weakening is nearly 13 A at a freestream velocity of 5 m/s, and decreases as freestream velocity increases. The difference between efficiency also decreases as freestream velocity increases, which can be seen in Figure 4.24 and favors the use of field weakening at higher freestream velocities.

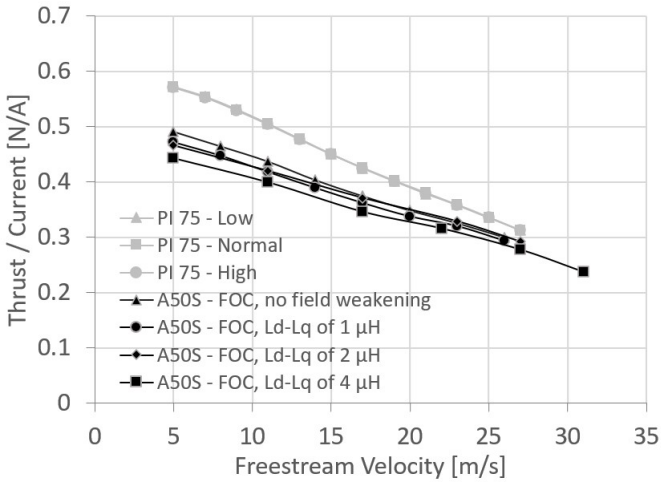

Figure 4.24: Wind tunnel full throttle $Thrust/Current$ as function of freestream velocity for the 7 configurations tested with the Aeronaut propeller and both ESCs.

The RPM values measured using the optical RPM sensor are shown in 4.25. There is a difference between the RPMs using different motor timings on trapezoidal control, but it is very small compared to the RPM increase caused by field weakening, which is really notorious.

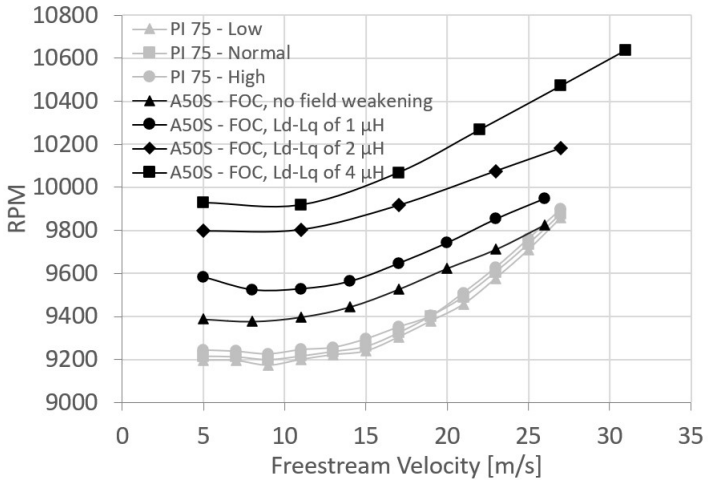

Figure 4.25: Wind tunnel full throttle RPM as function of freestream velocity for the 7 different configurations tested with the Aeronaut propeller and both ESCs.

4.2.5 Uncertainty Analysis

The results of the uncertainty analysis for the experiments using the Aeronaut propeller with the Phoenix ICE 75 on High Timing and the Triforce A50S with $Ld - Lq$ of 4 µH are shown in Table 4.1 and Table 4.2, respectively. The observed uncertainties prove to be small. It can be seen that V and J remain nearly constant because the uncertainty of the primary measurement $(p1 - p2)$ is relative, and increases as $(p1 - p2)$ increases. In the case of C_T and C_P, their uncertainty increases as the measured values of thrust and torque decrease.

	Uncertainty			
V_{target} [m/s]	V	J	C_T	C_P
5	0.2283%	0.2346%	0.5115%	0.3817%
7	0.2283%	0.2346%	0.5216%	0.3818%
9	0.2283%	0.2346%	0.5353%	0.3820%
11	0.2283%	0.2346%	0.5515%	0.3821%
13	0.2283%	0.2346%	0.5735%	0.3825%
15	0.2283%	0.2346%	0.6004%	0.3831%
17	0.2283%	0.2345%	0.6341%	0.3842%
19	0.2283%	0.2344%	0.6809%	0.3863%
21	0.2283%	0.2343%	0.7339%	0.3886%
23	0.2283%	0.2341%	0.8076%	0.3925%
25	0.2283%	0.2340%	0.9132%	0.3984%
27	0.2283%	0.2338%	1.0640%	0.4079%

Table 4.1: Uncertainty analysis relative to the setup with the Aeronaut propeller and the Phoenix ICE 75 on High Timing.

	Uncertainty			
V_{target} [m/s]	V	J	C_T	C_P
5	0.2277%	0.2332%	0.4733%	0.3727%
11	0.2277%	0.2332%	0.5002%	0.3731%
17	0.2277%	0.2331%	0.5513%	0.3737%
22	0.2277%	0.2329%	0.6311%	0.3765%
27	0.2277%	0.2327%	0.8063%	0.3856%
31	0.2277%	0.2325%	1.1879%	0.4078%

Table 4.2: Uncertainty analysis relative to the setup with the Aeronaut propeller and the Triforce A50S with $Ld - Lq$ of 4 µH.

Chapter 5

Concluding Remarks

The experimental study of an electric propulsion system with prescribed battery voltage and motor for two different propellers and two different ESCs with various settings under static and with relative wind condition was performed and documented. Sensorless trapezoidal commutation and sinusoidal FOC with and without field weakening along with various ESC configurations were tested. The desired objectives were achieved and the obtained results were very positive, given that field weakening allowed to vastly increase the thrust generated by the motor and propeller combination, specially at higher relative wind velocities, which was the main goal of the study.

In static conditions, the Triforce A50S with FOC and field weakening ($Ld - Lq$ of 4 µH) was able to produce 12.3% more static thrust than the best result achieved with the Phoenix ICE 75 (16 kHz PWM rate and high motor timing) and the Aeronaut propeller. With 5 m/s, 17 m/s and 27 m/s relative wind speed, the Triforce A50S with FOC and field weakening ($Ld - Lq$ of 4 µH) was able to produce 16.8%, 24.2% and 38.5% more thrust than the Phoenix ICE 75 (12 kHz PWM rate and high motor timing) with the same propeller. Furthermore, at 31 m/s, the Triforce A50S with FOC and field weakening ($Ld - Lq$ of 4 µH) was still able to produce 4.41 N of thrust, which is a very auspicious result.

Particularly for the ACC 2021/2022 competition, the recommended propeller is the Aeronaut 10x6 propeller. Although it has the same diameter and pitch as the APC 10x6, it is better at generating thrust and is more efficient at wind speeds above 16 m/s. The recommended ESC is the Triforce A50S because it has FOC and field weakening implemented. However, to use it in flight, a heat sink should be installed to improve its heat dissipation properties. Recently, the version 2.1 of this ESC was made available, and although it appears that the thermal properties have not been improved, the possibility of upgrading should be considered.

5.1 Future Work

As future work, it is suggested to perform limit testing of field weakening, in an attempt to squeeze the maximum possible thrust out of the given motor and propeller combination. Also, testing out the newer version of the Triforce A50S ESC is encouraged.

Bibliography

[1] AkaModell München. *Air Cargo 2022 Website*. 2021. URL: https://akamodell-muenchen.de/acc-2022/.

[2] Aaron M. Harrington and Christopher Kroninger. *Characterization of Small DC Brushed and Brushless Motors*. Army Research Laboratory, 2013.

[3] ON Semiconductor. *DC Motor Driver Fundamentals*. Semiconductor Components Industries, 2014.

[4] Rithvik Gambhir and Akshay Kumar Jha. "Brushless DC Motor: Construction and Applications". In: *The International Journal Of Engineering And Science (IJES)* (2013).

[5] Dejan. *How Brushless Motor and ESC Work*. 2019. URL: https://howtomechatronics.com/how-it-works/how-brushless-motor-and-esc-work/.

[6] Mark Drela. *First-Order DC Electric Motor Model*. MIT Aero and Astro, 2007.

[7] Ward Brown. *Brushless DC Motor Control Made Easy*. Microchip Technology Inc, 2019.

[8] Jorge Miguel Guedes Rebelo. "Development of an Efficient Propulsion System for a Battery Electric Shell Eco Marathon Prototype Vehicle". MSc Thesis. University of Beira Interior, 2017.

[9] Shane W. Colton. "Design and Prototyping Methods for Brushless Motors and Motor Control". MSc Thesis. Massachusetts Institute of Technology, 2008.

[10] Shiyoung Lee and Tom Lemley. *A Comparison Study of the Commutation Methods for the Three-Phase Permanent Magnet Brushless DC Motor*. 2015.

[11] Markos Tawadros, Jamal Rizk, and Mahmood Nagrial. "Sensorless Control of Brushless Drives Using Back emf Mapping". In: *Second International Conference on Computer and Electrical Engineering* (2009).

[12] Berrezzek Farid and Omeiri Amar. "A Study of New Techniques of Controlled PWM Inverters". In: *European Journal of Scientific Research* (2009).

[13] Kristen N. Mogensen. "Motor-control considerations for electronic speed control in drones". In: *Analog Applications Journal* (2016).

[14] NXP Semiconductors. *3-Phase Sensorless BLDC Motor Control Kit with S32K144*. 2020.

[15] Nuno Miguel Gomes da Silva. "Synchronous Wound-Rotor Electrical Machine Control for Electric Airplane Taxiing". MSc Thesis. Instituto Superior Técnico, 2011.

[16] Jorge Zambada and Debraj Deb. *Sensorless Field Oriented Control of a PMSM*. Application note. 2010.

[17] Texas Instruments Europe. *Field Orientated Control of 3-Phase AC-Motors*. 1998.

[18] Microsemi Corporation. *Field Oriented Control of Permanent Magnet Synchronous Motors*. Manual. 2012.

[19] Michael Thomas Ratcliffe and Kelum Akurugoda Gamage. "BLDC Motor Power Control Techniques Appraisal". In: *4th International Conference on Power Engineering, Energy and Electrical Drives* (2013).

[20] Muyang Li. "Flux-Weakening Control for Permanent-Magnet Synchronous Motors Based on Z-Source Inverters". MSc Thesis. Marquette University, 2009.

[21] Mathworks. *Field-Weakening Control (with MTPA) of PMSM*. 2020. URL: https://www.mathworks.com/help/mcb/gs/field-weakening-control-mtpa-pmsm.html.

[22] Alessandro Bosso et al. "A Computational-Effective Field-Oriented Control Strategy for Accurate and Efficient Electric Propulsion of Unmanned Aerial Vehicles". In: *IEEE/ASME TRANSACTIONS ON MECHATRONICS* (2020).

[23] Hastanto SM Widodo et al. "Approaching the Ideal BLDC Motor: A Novel Electronic Speed Controller System for a Generator-Converted BLDC Motor with Field Weakening Feature". In: *Modern Applied Science; Vol. 14* (2020).

[24] S. Senol and O. Ustun. "Young Tae Shin and Ying-Khai Teh". In: *IEEE 8th Annual Computing and Communication Workshop and Conference* (2018).

[25] S. Senol and O. Ustun. "Study on a BLDC Motor Having Higher Winding Inductance: a Key to Field Weakening". In: *XXth International Conference on Electrical Machines* (2012).

[26] *AXI Model Motors*. URL: https://www.modelmotors.cz/.

[27] Benjamin Vedder. *VESC Project*. 2021. URL: https://vesc-project.com/.

[28] Pedro Jorge Ferreira Alves. "Low Reynolds Number Propeller Performance Measurement in Wind Tunnel Test Rig". MSc Thesis. University of Beira Interior, 2014.

[29] W. J. Devenport and A. Borgoltz. *BASIC CONCEPTS IN EXPERIMENTS*. 2016. URL: http://www.dept.aoe.vt.edu/~aborgolt/aoe3054/manual/ch2/index.html.